

Solidification and Turbulence (Non-laminar) during Magma Ascent: Insights from 2D and 3D Analyses of Bubbles and Minerals in an Etnean Dyke

Gabriele Lanzafame^{1*}, Gianluca Iezzi^{2,3}, Lucia Mancini¹, Federica Lezzi², Silvio Mollo⁴ and Carmelo Ferlito⁵

¹Elettra-Sincrotrone Trieste S.C.p.A., SS 14, Km 163.5 in Area Science Park, 34149 Basovizza (Trieste), Italy;

²Dipartimento di Ingegneria & Geologia, Università G. d'Annunzio, Via dei Vestini 30, 66100, Chieti, Italy; ³Istituto Nazionale di Geofisica e Vulcanologia, Via di Vigna Murata 605, 00143, Roma, Italy; ⁴Dipartimento di Scienze della Terra, Sapienza-Università di Roma, P.le Aldo Moro 5, 00185 Roma, Italy; ⁵Dipartimento di Scienze Biologiche, Geologiche e Ambientali, Università di Catania, Corso Italia 57, I-95129 Catania, Italy

*Corresponding author. E-mail: gabriele.lanzafame@elettra.eu

Received December 12, 2016; Accepted September 27, 2017

ABSTRACT

Solidification, emplacement and fluid dynamics of a sub-volcanic rock at Mt Etna have been investigated through two-dimensional (2D) and three-dimensional (3D) textural analyses of the hosted bubbles and minerals. This rock is a 4.3 m thick aphyric dyke (DK) that solidified at a depth of 100–300 m, below the pristine surface level. Seven samples from the dyke rim (DK1) to core (DK7) have been analysed in two dimensions by using a high-resolution scanner, a transmission optical microscope and scanning electron microscopy imaging with back-scattered electrons, and in three dimensions by microfocus X-ray computed tomography. Field observations and mesoscopic polished rock surfaces show bubble-rich, -poor and -free patches even in rock pieces of a few cubic centimetres, with changes in sizes and shapes; even so, their shapes and spatial arrangement can never be attributed to high degrees of strain. In parallel, the amount of bubbles irregularly varies from dyke rim to core, whereas plagioclase (plg), clinopyroxene (cpx), titanomagnetite (timt), and olivine (ol) show only limited variations. The fabric of bubbles retrieved by 3D orientation of their maximum length (i.e. elongation) is invariably random in space for each DK sample. These bubble features have been attributed to transitional to turbulent flows; that is, non-laminar regimes (Reynolds number > 1000), predicted for a long time from numerical models and that occurred before the crystallization of minerals. Water solubility, volume of bubbles, magma density and viscosity models indicate that, at pressure higher than 10 MPa, 1 wt % H₂O was dissolved in the original trachybasaltic magma, which, in turn, was close to its liquidus temperature. As the pressure decreased at very shallow levels, the magma significantly degassed and volatile exsolution induced marked crystallization (mostly plg followed by cpx). The viscosity of the system increased, decelerating and halting the magmatic suspension. The textures and fabrics of bubbles were suddenly frozen in, despite crystals continuing to grow under the effect of cooling rate variables from the inner (DK7) to outer (DK1) dyke portions. Fluid-dynamic computations suggest that the DK trachybasaltic magma ascended with a velocity of few metres per second in a transitional to turbulent regime, before the growth of minerals.

Key words: dyke; bubbles; X-ray microtomography; turbulence (non-laminar); solidification

INTRODUCTION

The ascent of magmas to shallow crustal levels occurs mainly along dykes, which are categorized as discrete, vertical, sheet-like bodies. When the pressure at the top of a magmatic reservoir overcomes the tensile resistance of the overlying rocks, failures can develop by coalescence of cracks under stress induced by pressurized volatiles (gas cap of H_2O and CO_2) and fluids (melt \pm dissolved volatiles \pm minerals \pm bubbles). Failures then propagate upwards responding to the mechanical properties of the overlying rocks, regional and local stress fields, and the fluid-mechanical behaviour of injected magmas (Pollard, 1973, 1976, 1987; Spera, 1980; Delaney *et al.*, 1986; Lister & Kerr, 1991; Rubin, 1995; Gudmundsson *et al.*, 1999; McLeod & Tait, 1999; Menand & Tait, 2001; Gudmundsson, 2006; Acocella & Neri, 2009; Geshi & Neri, 2011; Daniels *et al.*, 2012; Maimon *et al.*, 2012; Mangan *et al.*, 2014; Gonnerman & Taisne, 2015; Rivalta *et al.*, 2015; and references therein).

Most dykes develop near-vertically in the host rocks and, rarely, produce eruptions. This depends on the physico-chemical conditions of the magma and its host-rock, such as the bulk composition, temperature (T), pressure (P), volatile and/or mineral contents, as well as kinetic effects dictating crystal nucleation and growth, degassing, and outgassing. Kinetic effects are governed by heat transfer from the magma to the surrounding host-rock and the ascent rate imposed by magmatic overpressure and density contrast between the magma and cross-cut rock(s) (Spera, 1980; Bruce & Huppert, 1990; Carrigan *et al.*, 1992; Rubin, 1995; Carrigan, 2000; Jaupart, 2000; Pinel & Jaupart, 2004; Taisne & Jaupart, 2009; Maccaferri *et al.*, 2011; Taisne *et al.*, 2011; Zuan Chen *et al.*, 2011; Maimon *et al.*, 2012; Yamato *et al.*, 2012, 2015; Mangan *et al.*, 2014; Gonnerman & Taisne, 2015; Rivalta *et al.*, 2015; and references therein).

Theoretical aspects of dyke emplacement, such as the central topic concerning fluid-dynamic regimes in dykes (Maccaferri *et al.*, 2011; Galindo & Gudmundsson, 2012; Daniels *et al.*, 2014; Gonnerman & Taisne, 2015; Rivalta *et al.*, 2015), require corroboration by field and petrological data. In this context, theoretical and numerical models predict both laminar and non-laminar regimes (Huppert & Sparks, 1985; Emerman & Turcotte, 1986; Spence & Turcotte, 1990; Carrigan, 2000; Jaupart, 2000), but turbulence in dykes has only been suggested based on crude field observations (Kille *et al.*, 1986).

Pioneering two-dimensional (2D) textural and fabric studies of minerals and bubbles have unveiled both petrological and rheological magmatic processes in dykes (Teall, 1884; Queneau, 1902; Holmes & Larwood, 1929; Quinn, 1943; Winkler, 1948; Campbell & Schenk, 1950; Cashman, 1992; Sigurdsson, 2000; Mangan *et al.*, 2014). These studies were followed by more quantitative 2D investigations (Gray, 1970, 1978; Komar, 1972, 1976; Ikeda, 1977; Howard, 1980; Shelley, 1985; Wada, 1992; Hastie *et al.*, 2011, 2013), revealing variations in the size and shape of minerals and bubbles, as well as in the

fabric moving from the central to the external parts of dykes. In recent decades, dykes have been largely investigated by three-dimensional (3D) anisotropic magnetic susceptibility (AMS) (Ernst & Baragar, 1992; Callot *et al.*, 2001; Herrero-Bervera *et al.*, 2001; Femenias *et al.*, 2004; Aubourg *et al.*, 2008; Eriksson *et al.*, 2011; Bjarne *et al.*, 2012; Andersson *et al.*, 2016; and references therein) and to a lesser extent by 2D textures combined with magnetic properties (Poland *et al.*, 2004; Clemente *et al.*, 2007; Philpotts & Philpotts, 2007; Hastie *et al.*, 2013). Conversely, a few studies on volcanic rocks have been performed using other 3D methods to investigate crystal lattice preferred orientation such as electron backscatter diffraction (EBSD) (Bascou *et al.*, 2005), neutron diffraction (Walter *et al.*, 2013) and X-ray computed microtomography (μ CT) (Álvarez-Valero *et al.*, 2016).

The orientation of magnetic tensors mainly depends on the texture and fabric of iron-bearing crystals with relevant magnetic signals such as titanomagnetite (tmt), with a moderate effect for biotite (bt) and amphibole (amph), and a low effect for plagioclase (plg), clinopyroxene (cpx) and olivine (ol). Hence, AMS may be not suitable to measure absolute dimensions and shapes of bubbles and the whole mineral phases, recording only the late stage of deformation (Iezzi & Ventura, 2002; Cañón-Tapia & Chaves-Álvarez, 2004; Cañón-Tapia & Herrero-Bervera, 2009). Magma dynamics in dykes can also be successfully investigated by variations in mineral compositions (e.g. Chistyakova & Latypov, 2009; Tartese & Boulvais, 2010; Mollo *et al.*, 2011, 2012; Scarlato *et al.*, 2014). The combination of texture, fabric, and composition of each phase is the most complete strategy to reconstruct the solidification paths of magmas feeding dykes. Unfortunately, dykes are scarcely investigated by modern microchemical and 2D imaging methods, as well as 3D imaging techniques. Only recently has X-ray μ CT been applied to dacitic magmas (Álvarez-Valero *et al.*, 2016), which have obvious compositional, textural, and rheological differences from the trachybasaltic magma analyzed here.

In this study, the textural and fabric attributes of seven rock samples representative of the internal variability of an Etnean dyke from rim to core have been investigated to complement major and trace element changes previously documented for plg, cpx and tmt (Mollo *et al.*, 2011; Scarlato *et al.*, 2014). The rock samples have been analyzed by 2D methods (on polished rock surfaces and thin sections) and 3D imaging using laboratory X-ray μ CT. The size, shape, and orientation of bubbles and minerals allow us to reconstruct the solidification behaviour of the magma and appear to confirm the fluid-dynamic scenario suggested by theoretical models. Similar investigations can be extended to other dykes or lavas to better understand the mechanisms responsible for the transport of magmas at shallow crustal levels and in volcanic eruptions.

THE ETNEAN DYKES

Geological setting

Mt Etna is an active stratovolcano located in eastern Sicily (Italy) and is characterized by effusive and Strombolian activity associated with persistent degassing from its four main craters (Monaco *et al.*, 1997; Ferlito & Lanzafame, 2010; Ferlito *et al.*, 2014). The main edifice of the volcano was built in the last 220 kyr (Gillot *et al.*, 1994; Tanguy *et al.*, 1997, 2007; De Beni *et al.*, 2005; Branca *et al.*, 2008) and developed through four major phases: Ancient Alkaline Centers (AAC; 220–120 ka), Trifoglietto (80–60 ka), Ellittico (60–15 ka) and Recent Mongibello (15 ka to present) (Cristofolini *et al.*, 1979; Romano, 1982; Gillot *et al.*, 1994; Catalano *et al.*, 2004; Monaco *et al.*, 2005; and references therein). On its eastern side the current edifice is characterized by the Valle del Bove depression, bordered on its western part by the high reaches of the volcano and on its northern and southern sides by steep walls formed by remains of the Trifoglietto and Ellittico products (McGuire, 1982; Romano, 1982; Lanzafame & Vestch, 1985; Ferlito & Cristofolini, 1989; Calvari *et al.*, 1994; Coltellini *et al.*, 1994; D’Orazio *et al.*, 1997; Monaco *et al.*, 2010). Several dykes crop out over these steep walls, displaying portions of the ancient shallow plumbing system feeding the various eruptive centres (see Ferlito & Nicotra, 2010).

Features and sampling of the dyke

On the southern wall of the Valle del Bove, at the head of the wide gully named Canalone dei Faggi at about 1700 m a.s.l. (Fig. 1), several dykes are observable with common features: thickness of a few metres, near-vertical attitude, sharp contacts with wall-rocks, absence or very limited content of observable crystals (aphanitic texture), and moderate amounts of slightly deformed bubbles distributed in bubble-rich, -poor and -free patches. The bubbles do not follow any textural trends from rim to core and primarily form eddies or vortices with diameters from several centimetres to a few decimetres.

We focused on a 4.3 m thick dyke (i.e. DK), which intruded lava and pyroclastic sequences ascribed to the Ellittico activity before 15 ka. This portion of the dyke was originally located at a depth of 100–300 m below the ground surface (Mollo *et al.*, 2011). According to the field characteristics of the DK outcrop (Fig. 1), the dyke was emplaced in a single magmatic pulse, because of its very sharp contacts, absence of any engulfment of wall-rocks and systematic chemical variations of minerals from rim to core (Mollo *et al.*, 2011). From outermost to innermost DK portions, seven samples, DK1 to DK7, were collected with a sampling distance of ~350 mm. These prismatic samples were oriented coaxially to the field: z is the vertical direction, x is the thickness (rim to rim) and y is the horizontal direction of DK (Fig. 1). The sampled rocks have edges of about 100–200, 100–200 and 50–100 mm. Each sample was cut normally to the

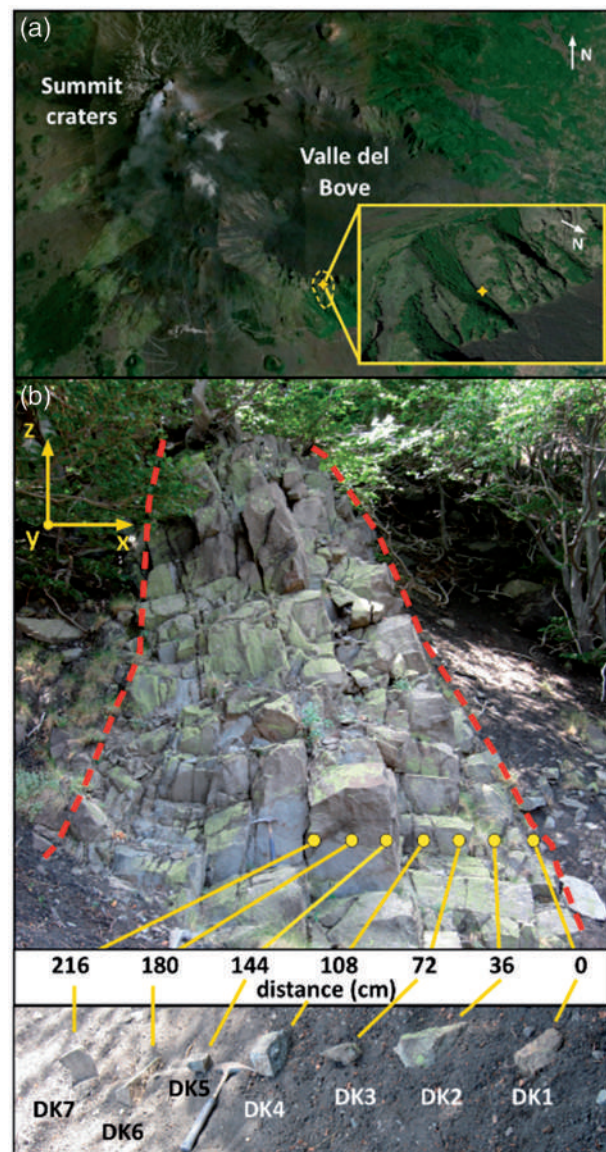


Fig. 1. (a) Location of the dyke (yellow star) and Canalone dei Faggi (yellow dashed line); Google Earth image (b) The dyke characteristics in the field, with lateral contacts (red dashed lines) and the position and orientation of the DK samples. z, x and y are vertical, rim-to-rim (thickness) and normal to the plane dyke directions, respectively.

dyke walls such as to expose the representative z–x surfaces (Fig. 1), then seven surfaces (or portions of them) with areas in the order of 10^3 – 10^4 mm 2 were polished for statistically significant mesoscopic observations. The short and long sides of these sections are coaxial with the z and x directions, respectively. We collected these samples in the half-width right part of the dyke, assuming that the rocks are representative of the entire dyke. Although some dykes may show a non-symmetrical fabric from rim to rim (Femenias *et al.*, 2004; Nkono *et al.*, 2006), the small overall thickness of the dyke presented in this study ensures symmetrical characteristics.

Mineralogy and geochemistry

The seven rock samples that are the object of this study have been previously investigated by Mollo *et al.* (2011, 2013) and Scarlato *et al.* (2014). The DK dyke is trachybasaltic with (wt %) $\text{SiO}_2 = 48.6 (\pm 0.3)$, $\text{TiO}_2 = 1.9 (\pm 0.1)$, $\text{Al}_2\text{O}_3 = 16.9 (\pm 0.2)$, $\text{FeO} = 11.3 (\pm 0.2)$, $\text{MnO} = 0.2 (\pm 0.1)$, $\text{MgO} = 4.2 (\pm 0.1)$, $\text{CaO} = 10.4 (\pm 0.1)$, $\text{Na}_2\text{O} = 3.8 (\pm 0.2)$, $\text{K}_2\text{O} = 1.6 (\pm 0.1)$ and $\text{P}_2\text{O}_5 = 1.2 (\pm 0.1)$. The phase assemblage of the dyke comprises cpx, plg, and tmt, plus ol xenocrysts (Mollo *et al.*, 2011). Plg, cpx and tmt compositions progressively change from dyke core to rim (Mollo *et al.*, 2011, 2013). Specifically, albite (Ab), diopside (Di) and ulvöspinel (Usp) contents increase, counterbalanced by a decrease of anorthite (An), Tschermark (Ts) and magnetite (Mg) (Supplementary Data Fig. 1S; supplementary data are available for downloading at <http://www.petrology.oxfordjournals.org>). The increasing amounts of Ts from dyke core to rim are also accompanied by increasing concentrations of rare earth elements (REE) in cpx (Supplementary Data Fig. 1S) (Scarlato *et al.*, 2014).

MATERIALS AND METHODS

2D imaging, processing, and analysis

The mesoscopic polished surfaces with areas ranging from 10^3 to 10^4 mm^2 were prepared to expose phases with maximum dimension $>1 \text{ mm}$. Thin sections show 2D textural attributes at the 1:1 scale, acquired by a high-resolution scanner (HRS), at $2.5\times$ and $10\times$ magnification (parallel and cross polarizers) with a transmission optical microscope (TOM) and at $100\times$ to $3000\times$ magnification by scanning electron microscope with back-scattered electrons (BS-SEM). HRS analyses were performed with a high-resolution Epson V750 Pro scanner and TOM investigations were carried out with a Zeiss Axioscope optical microscope, both installed at the Dipartimento di Ingegneria & Geologia of the University G. d'Annunzio (Chieti, Italy). For BS-SEM analyses a Jeol-JXA8200 scanning electron microscope, equipped with an energy-dispersive spectroscopy (EDS) probe and installed at the HPHT Laboratory of Experimental Volcanology and Geophysics of the Istituto Nazionale di Geofisica e Vulcanologia (INGV) in Rome (Italy) was used. Variable areas and related magnifications of digital images allowed us to constrain statistically all phases with sizes from centimetre to micrometre scale (down to $1 \mu\text{m}$), avoiding oversampling (excess counting of tiny objects) and undersampling effects (excess counting of large objects).

The techniques employed for textural quantification, on the basis of phase sizes, are summarized in Table 1. Nine images per sample with a total of 63 digital images were recorded, following the protocols and procedures reported in previous studies (Higgins, 2006; Iezzi *et al.*, 2008, 2011, 2014; Lanzafame *et al.*, 2013; Vetere *et al.*, 2013, 2015b). The 2D image processing and analysis were performed using Image Pro-Plus 5.0 Media

Cybernetics commercial software. Each image, obtained at various magnifications, was first transformed to grey levels (where zero is black and 255 is white) and calibrated to a millimetre scale. After the use of a 2D median filter to remove noise, each phase (bubbles and crystals) with its distinctive grey levels was identified. Thereafter, the phases were reproduced in false colours, segmented, and automatically counted.

Objects attributed to each phase were characterized considering their corresponding equal-area ellipses. We calculated the phase abundance expressed as area % (ratio between the area occupied by the investigated phase and the total area of the sample section), the areal number density (defined as the number of objects per unit area, no. mm^{-2}), the object size in terms of aspect ratio (defined by the long and short axes of their equal-area ellipses and their ratio), and the orientation of the long axis with respect to the x direction (see Fig. 1).

Bubbles having sizes $>0.1 \text{ mm}$ were quantified by means of images from HRS and TOM. Because crystal sizes never exceed $\sim 0.2 \text{ mm}$ they were measured on BS-SEM images (see below). Plg phases aggregate along their longest axis, preventing the accurate identification of single crystals and thus providing only their phase abundances (area %). In contrast, cpx, tmt, and ol phases occur mainly as single crystals, with only some of them showing aggregation features. Consequently, we assumed that agglomerated grains invariably correspond to a single crystal (see Fig. 2). Bubbles can be sharply identified and quickly measured as single objects. A schematic view of the 2D image processing and analysis protocol is represented in Fig. 2.

3D imaging, processing, and analysis

Seven DK samples with dimensions from 4.2 to 10.8 cm^3 (see Table 2) were cut and imaged by laboratory X-ray μ CT using the TomoLab station at the Elettra synchrotron light facility in Basovizza (Trieste, Italy) (Mancini *et al.*, 2007; Polacci *et al.*, 2009). The TomoLab is equipped with a sealed microfocus X-ray tube operating in a voltage range from 40 to 130 kV, a maximum current of $300 \mu\text{A}$ and a minimum focal spot size of $5 \mu\text{m}$. The used detector consisted of a full frame CCD imager (4008×2672 pixels) coupled to a gadolinium oxysulphide scintillator by a fiber-optic tape. The water-cooled CCD camera has a 12-bit dynamic range, and an effective pixel size of $12.5 \times 12.5 \mu\text{m}^2$. Owing to the cone-beam geometry, it is possible to achieve a spatial resolution close to the focal spot size, on samples from a few millimetres to a few centimetres in size. The experimental parameters used for the X-ray μ CT scans are reported in Table 2. Scans for DK1 and DK5 were acquired with a pixel size of $6.25 \mu\text{m}$, whereas for samples DK2, DK3, DK4, DK6 and DK7 a pixel size of $8 \mu\text{m}$ was set. The slice reconstruction was performed using the commercial software COBRA (Exxim) based on the

Table 1: Two-dimensional textural results

Sample label	Distance from wall-rock (cm)	Phase	>1 mm (area %) (HRS)	>0.1 and ≤1 mm (area %) (TOM)	<0.1/0.2 mm (area %) (BS-SEM)	2D whole amount (area %)	No. mm ⁻²
DK1	0	bubbles	0.4	10.8 (3.2)	—	11.2	3.50
		plg	—	—	72.1 (1.7)	72.1	—
		cpx	—	—	22.3 (1.4)	22.3	4113
		ol	—	—	1.8 (0.8)	1.8	1076
		timt	—	—	3.9 (0.9)	3.9	1192
DK2	36	bubbles	10.5	9.1 (3.4)	—	19.6	0.69
		plg	—	—	72.1 (2.3)	72.1	—
		cpx	—	—	20.6 (2.8)	20.6	2491
		ol	—	—	2.5 (0.4)	2.5	1097
		timt	—	—	4.9 (0.8)	4.9	727
DK3	72	bubbles	5.4	3.6 (4.5)	—	8.9	0.31
		plg	—	—	71.0 (2.4)	71	—
		cpx	—	—	17.9 (1.6)	17.9	2651
		ol	—	—	3.3 (0.7)	3.3	1812
		timt	—	—	7.7 (1.6)	7.7	1401
DK4	108	bubbles	13.6	12.8 (3.5)	—	26.4	0.90
		plg	—	—	71.3 (2.4)	71.3	—
		cpx	—	—	19.0 (1.1)	19	1853
		ol	—	—	5.1 (1.0)	5.1	1280
		timt	—	—	4.8 (0.8)	4.8	441
DK5	144	bubbles	27.4	1.6 (2.1)	—	29	0.21
		plg	—	—	67.5 (2.5)	67.5	—
		cpx	—	—	18.8 (1.8)	18.8	1443
		ol	—	—	6.8 (2.2)	6.8	1291
		timt	—	—	6.9 (1.4)	6.9	680
DK6	180	bubbles	8.5	0.7 (0.8)	—	9.2	0.15
		plg	—	—	67.3 (0.8)	67.3	—
		cpx	—	—	20.6 (2.4)	20.6	1349
		ol	—	—	6.8 (0.9)	6.8	1609
		timt	—	—	5.4 (0.9)	5.4	426
DK7	216	bubbles	20.9	1.3 (1.4)	—	22.2	0.23
		plg	—	—	70.7 (3.6)	70.7	—
		cpx	—	—	19.7 (2.6)	19.7	1423
		ol	—	—	5.5 (0.5)	5.5	1614
		timt	—	—	3.9 (0.6)	3.9	423

Crystals were measured only by BS-SEM, whereas bubbles were measured only by HRS and TOM owing to their sizes >0.1 mm.

Feldkamp algorithm (Feldkamp *et al.*, 1984). The same software allowed us to correct beam hardening artefacts (Kitchen *et al.*, 2007).

The 3D image processing and analysis of the seven imaged samples were performed using the *Pore3D* software library developed at Elettra (Elettra, 2009; Brun *et al.*, 2010; Zandomeneghi *et al.*, 2010), which allows extraction of quantitative microstructural and textural parameters of porous and multiphase systems. The software includes tools for filtering and segmentation of digital images, and procedures for the analysis of morphology, texture and anisotropy, as well as for the skeletonization and skeleton analysis functions to extract topological information. The *Pore3D* software was also used to reduce ring artefacts from the reconstructed axial slices (Sijbers & Postnov, 2004; Brun *et al.*, 2011). The 3D visualization (through surface and volume rendering procedures) of reconstructed and processed volumes was done employing the commercial software VGStudio MAX 2.0 (Volume Graphics).

The image acquisition protocol adopted for the X-ray μ CT imaging in this study allows the investigation of bubbles at medium ($\sim 10 \mu\text{m}$) spatial resolution on

centimetre-sized samples. For that reason, we worked in absorption mode and this did not allow us to characterize tiny crystals, such as ol, plg and cpx, with refractive indices close to the rock matrix. Conversely, it was possible to investigate fully, within the limit of the selected spatial resolution, the morphological and textural features of timt crystals, owing to the high contrast of this phase with respect to the rock sample matrix.

The quantitative analysis was performed on suitable Volumes of Interest (VOIs), extracted from each imaged sample with the aim of detecting all the representative structures of the rocks (Table 3). To verify the representativeness of the selected VOIs, Representative Elementary Volumes (REVs) were determined. An REV is defined as the minimum volume large enough to enclose a significant amount of the sample heterogeneity (Gitman *et al.*, 2007; Zandomeneghi *et al.*, 2010). For each sample, we considered the bubble and timt volume fraction as the parameter for REV determination applying the box-counting method (Al-Raoush & Papadopoulos, 2010; Zhang *et al.*, 2012).

VOIs having size larger than the determined REVs were extracted and then filtered to remove noise and

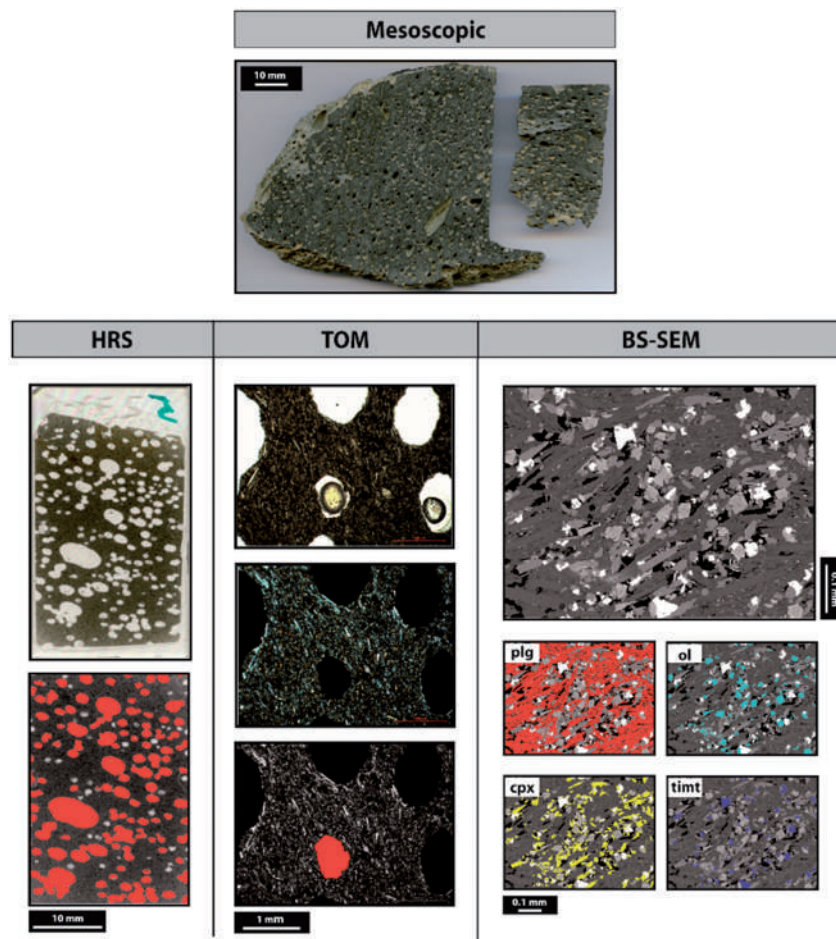


Fig. 2. Examples of 2D observation and segmentation of phases by image analysis. Top: mesoscopic polished surface (DK5) used for general inspection of large phases and their disposition in space. Lower left: high-resolution scanner (HRS) original scanned image (above) and its corresponding segmented image (below) used for counting phases >1 mm in size (in red). Lower middle: transmission optical microscopy (TOM) parallel and cross-polarized digital images at $2.5\times$ (above and middle) with segmented phases >0.1 and ≤1 mm in size (in red) (below). Lower right: back-scattered scanning electron microscopy (BS-SEM) image at $200\times$ (above) and the corresponding segmented phases with size <0.2 mm (below). False colours on HRS, TOM and BS-SEM images are red for bubbles, yellow for cpx, cyan for ol, and blue for timt (red is used for plg only in BS-SEM images). In this dyke, bubbles with size <0.1 mm are not observed or are extremely rare, whereas the single crystal length is ≤0.2 mm.

Table 2: Three-dimensional analytical conditions

Sample label	d_1 (mm)	d_2 (mm)	Volume (cm^3)	Tube voltage (kV)	Current (μA)	Filter	Voxel size (μm)	No. of projections	Angle of rotation (deg)	Exposure time (s)
DK1	100	400	10.8	130	61	1.5 mm Al	6.25	2400	360	6.5
DK2	80	250	5.3	130	61	1.5 mm Al	8	1800	360	4
DK3	80	250	3.8	130	61	1.5 mm Al	8	1800	360	4
DK4	80	250	10.1	130	61	1.5 mm Al	8	1800	360	4
DK5	100	400	4.2	130	61	1.5 mm Al	6.25	2400	360	6.5
DK6	80	250	6.2	130	61	1.5 mm Al	8	1800	360	4
DK7	80	250	6.3	130	61	1.5 mm Al	8	1800	360	4

Experimental parameters used for the X-ray μ CT scans. d_1 , source to sample distance; d_2 , source to detector distance.

preserve edges using an ‘anisotropic diffusion filter’ (Weickert, 1998). The next step was the segmentation of the images to obtain binary volumes containing the different classes of the phases of interest. Thresholding was performed using the automatic MultiOtsu method (Otsu, 1979). For each sample, we extracted two binary datasets corresponding to bubbles and timt, the least

and most dense phases with respect to the DK groundmass. Segmented images were then processed applying various cycles of erosion and dilation to remove noise and background objects $<3\text{--}5$ voxels (Serra, 1982).

Because samples show bubbles and timt in contact with the border of the VOIs, analyses were performed

Table 3: Three-dimensional textural results

Sample label:	DK1	DK2	DK3	DK4	DK5	DK6	DK7
Voxels	651 × 516 × 857	796 × 1122 × 1270	826 × 990 × 1280	667 × 1374 × 1280	468 × 1080 × 1270	598 × 916 × 1270	740 × 924 × 1270
Isotropic-voxel length (mm)	0.0063	0.0080	0.0080	0.0080	0.0063	0.0080	0.0080
Volume (mm ³)	70.3	580.7	535.9	600.6	156.7	356.2	444.6
Volume %	bubbles timt	10.9 2.48	16.8 2.80	12.2 2.65	13.9 2.89	22.9 2.63	10.8 2.59
Number	bubbles timt	4143 6338	729 30470	2993 33356	781 47302	2495 17505	353 24965
Number per volume (no. mm ⁻³)	bubbles timt	58.9 90.2	1.3 52.5	5.6 62.2	1.3 78.8	15.9 111.7	1.0 70.1
Average volume (mm ³)	bubbles timt	0.002 2×10^{-4}	0.133 4×10^{-4}	0.022 4×10^{-4}	0.107 3×10^{-4}	0.014 2×10^{-4}	0.109 3×10^{-4}
Average aspect ratio	bubbles	0.25	0.38	0.33	0.35	0.22	0.36
Average sphericity	bubbles	0.69	0.71	0.71	0.72	0.71	0.73
Specific surface area (mm ⁻¹)	bubbles	4.5	0.6	0.6	0.3	0.1	0.2
Integral of mean curvature (mm ⁻²)	bubbles	53.1	2.3	4.5	1.1	2.5	0.9
Euler characteristic (mm ⁻³)	bubbles	51.9	0.7	4.5	0.9	15.5	0.7
Connectivity density	bubbles timt	-10.45 0.03	0.40 0.09	0.17 0.10	0.41 0.05	1.66 0.10	0.35 0.04
Elongation index	bubbles timt	0.03 0.06	0.09 0.06	0.07 0.07	0.06 0.06	0.02 0.02	0.04 0.04
Isotropy index	bubbles timt	0.73 0.93	0.74 0.88	0.70 0.89	0.71 0.90	0.78 0.90	0.71 0.90
							0.77 0.89

Average aspect ratio is the ratio between the longest and the shortest segment passing through the centre of mass. Average sphericity is the ratio of the diameter of the maximum inscribed sphere in a blob and the diameter of the sphere with the same volume as the blob. Specific surface area is the ratio between the surface of the objects and their volume. For the integral of mean curvature, positive and negative values indicate the dominance of convex and concave objects (bubbles) respectively. Euler characteristic is an index of connectivity of the object network (bubbles), where positive and negative values are indicative of isolated versus connected or aggregated objects (bubbles). Connectivity density is the number of redundant connections normalized to the total volume, with negative and positive values indicative of low and high connection respectively. Elongation index measures the preferred orientation of a fabric, varying between zero (no preferred orientation) and unity (perfect preferred orientation). Isotropy index measures the similarity of fabric to a uniform distribution, changing between zero (fully anisotropic) and unity (perfect isotropy).

on two datasets: (1) VOIs containing all the objects to quantify their total amount; (2) VOIs in which the objects touching the image margins were suppressed, considering only the morphometric values of un-truncated objects. We applied the *Basic Analysis* module of the *Pore3D* software (Zandomeneghi *et al.*, 2010) to obtain bubble and timt density (number of voxels of each phase versus the total number of voxels), specific surface area (surface area of all the phases divided by the total VOI), integral of mean curvature (an index of the abundance of convex versus concave shapes; Russ & DeHoff, 1986) and Euler characteristic (index scaling with the network connectivity of a given phase; Odgaard & Gundersen, 1993; Ohser & Mücklich, 2000). The results are reported in Table 3. All bubbles and timt crystals, identified using the concept of maximal inscribed spheres (Hildebrand & Rüegsegger, 1997; Baker *et al.*, 2012), were then labelled and analysed, calculating the number of elements, volume, sphericity, aspect ratio and diameter of the maximal inscribed sphere. The spatial relations of the objects within the samples were then investigated calculating the values of isotropic distribution (I) and preferential orientation (E) of bubbles and timt crystals.

The connectivity of bubble networks was investigated by a skeletonization approach (Lindquist & Lee, 1996). The skeleton can describe the connectivity and tortuosity of the bubble network, as it can be intuitively

considered as the 1D representation of the 'spine' of a 3D object. Owing to hardware-related computational limits, the skeletonization was performed on sub-VOIs with a size of 500 × 500 × 500 voxels, still having REV characteristics. Among the skeletonization algorithms available in *Pore3D* we selected the *LKC* skeletonization function (Lee *et al.*, 1994), which is particularly suitable for those volcanic samples characterized by limited connectivity of the bubble network. Two cycles of 3D median filtering were run on the segmented images of bubbles to smooth their borders before the computation. After skeletonization, an iterative pruning of all branches with sizes <20 voxels was applied. The application of smoothing and pruning procedures allowed removal of unnecessary branches and nodes, which, after visual inspection by the operator, are found to be not representative of the real connectivity frames. Once obtained, skeletons were used to calculate the connectivity density (CD), defined as a scalar value representing the number of redundant connections normalized to the total volume V and computed as

$$CD = (1 - X_V)/V$$

where $X_V = (n - b)$, n being the number of bubbles and b the number of bubble-to-bubble branches of the skeleton (Brun *et al.*, 2010). Negative CD values indicate scarce connection, whereas positive values are typical of highly connected networks (Brun *et al.*, 2010;

Zandomeneghi *et al.*, 2010). A graphical summary of the most important 3D image processing and analysis steps adopted is illustrated in Fig. 3.

RESULTS

The 2D textural features of phases are summarized in Fig. 4 and detailed information is reported in the Supplementary Data (Fig. S1–S7). From dyke rim (DK1) to core (DK7), the most important characteristics are as follows: (1) bubble size (long axis of equal-area ellipse) is >0.1 mm and crystal size is <0.1 mm for most of the minerals (only a few crystals have size exceeding 0.2 mm); (2) bubbles show heterogeneous distributions, shapes, and orientations that contrast with the high homogeneity of crystals; (3) the glass matrix is absent or possibly corresponds to only a few area per cent around plg rims (Fig. 4; Supplementary Data Fig. S1–S7).

Area per cent, size, number density, shape, and orientation of bubbles do not follow any monotonic trend (see Fig. 4, and Supplementary Data Fig. S1–S7). At the macroscopic scale, DK1 is the only sample containing a great number of sub-millimetric (size >0.1 and <1 mm) bubbles, whereas other samples are mostly characterized by larger bubbles (size >1 mm). Bubbles with smaller dimensions appear more equant than larger

ones. Bubbles in DK5 and DK7 have low aspect ratios and ellipsoid shapes. DK2 displays bubbles with highly anisotropic and irregular shapes, whereas intermediate shapes are observed in DK1, DK3, DK4 and DK6. The fabric of bubbles is oriented nearly coaxial to the vertical z direction (see Fig. 1) in DK2, DK4, DK5, and DK6, at 30/60° from z for DK3, and along x for DK6 (Fig. 4; Supplementary Data Fig. S1–S7). These observations from digital scanned images reflect those on the field and polished rock samples.

The texture and fabric of minerals display weak variations from dyke rim to core, in contrast to the texture of the bubbles (Fig. 4; Supplementary Data Fig. S1–S7). Plg is by far the most abundant phase and occurs mainly as attached crystals along their longest directions. Cpx is the second most abundant mineral, with prismatic contours and only a minor degree of attachment to itself. The amount of tmt is low, with only large crystals (maximum size of about 100 μm) exhibiting slight irregular boundaries, probably resulting from the attachment of tiny crystals (maximum size of a few micrometres). OI occurs invariably as small equant and faceted crystals (Fig. 4; Supplementary Data Fig. S1–S7).

The area per cent values of phases observed by HRS, TOM, and BS-SEM analyses conducted at different magnifications are summarized in Table 1 and plotted in Fig. 5a where the area per cent values of minerals are calculated on a bubble-free basis. The abundance of bubbles from dyke rim to core shows an irregular non-monotonic trend (Fig. 5a). Bubbles with size >1 mm are infrequent (0.1 area %) in DK1, whereas bubbles with size >0.1 mm and ≤ 1 mm are infrequent (<2 area %) in the inner dyke portions (DK5, DK6, and DK7) and more abundant (9.1–12.8 area %) in DK1, DK2, and DK4 (Table 1).

The values of plg area per cent show slight variation along the dyke profile similar to what is observed for cpx (Fig. 5a). The number density of cpx strongly decreases from DK1 to all other dyke samples (Table 1 and Fig. 5b). OI has a low abundance and a crystal length of a few tens of micrometres (Table 1; Fig. 4; Supplementary Data Fig. S1–S7).

The 3D bubble textural parameters are reported in Table 3 and are graphically represented in Fig. 6a and b. The volumetric abundance of bubbles follows a complex heterogeneous trend (Fig. 7a) similar to that determined by the 2D analysis (Fig. 5a). Samples DK1 and DK6 have the lowest bubble contents (~11 vol. %), whereas sample DK5 has the highest bubble amount (~23 vol. %). The abundance of bubbles obtained by 3D analysis is comparable with the 2D data for samples DK1, DK2, DK3, DK6 and DK7. In contrast, the 2D and 3D data show differences for samples DK4 and DK5 (see discussion below). The overall trend depicted by the number of bubbles per unit volume in three dimensions is similar to that measured in two dimensions (Figs 5b and 7b).

The 3D measurements show that the abundance (2.4–2.9 vol. %) of tmt remains practically constant from

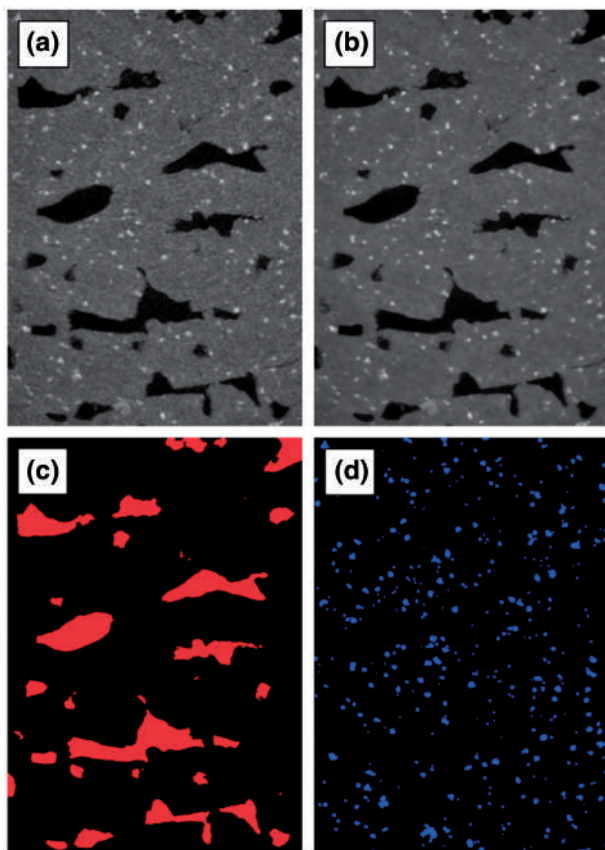


Fig. 3. Example of the Pore3D image analysis protocol applied to sample DK2. (a) Portion of a reconstructed axial slice; (b) filtered image with an 'anisotropic diffusion filter'; (c) threshold bubbles and (d) tmt by 3D MultiOtsu filtering.

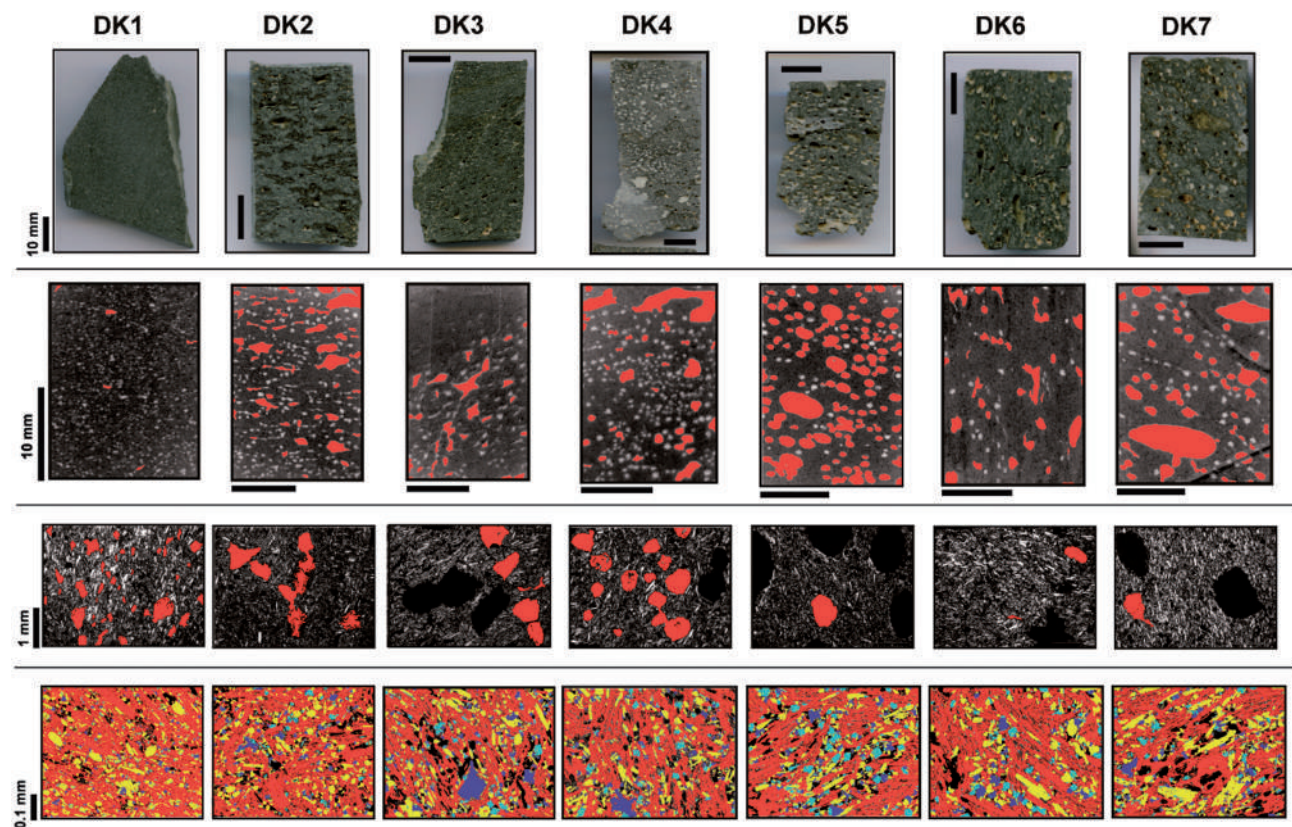


Fig. 4. Original and segmented textural features of DK samples at variable scales. First, second, third and fourth rows from top to down show: (1) mesoscopic attributes on polished rock surfaces ($\sim 10^3 \text{ mm}^2$); (2) HRS images of the polished thin sections ($\sim 10^2 \text{ mm}^2$); (3) TOM segmented images at $2.5\times$ ($\sim 10^1 \text{ mm}^2$); (4) BS-SEM segmented pictures ($\sim 10^{-1}$ to 10^{-2} mm^2). Bubbles have sizes $>0.1 \text{ mm}$ (red in second and third rows), whereas crystals (fourth row) have sizes $\leq 0.2 \text{ mm}$. Red, plg; yellow, cpx; cyan, ol; blue, tmt. The short and long edges of thin sections (second row) are coaxial with z and x directions (see Fig. 1). Further details are reported in Supplementary Data Fig. S1–S7.

dyke rim to core (Table 3), whereas the 2D data point to a larger variation from 3 area % (DK7) to 7 area % (DK3). However, the remaining samples (DK1, DK2, DK4, DK5 and DK6) have tmt very close to 4 area % (Table 1). From DK1 to DK7, the amount and number density of tmt are low, showing modest variations for both 2D (3.9–7.7 area % and 400–1100 no. mm^{-2}) and 3D methods (2.48–2.89 vol. % and 52–112 no. mm^{-3}) (see Tables 1 and 3; Figs 4–8; Supplementary Data Fig. S1–S7). The distribution of tmt is almost homogeneous in the samples ($I \geq 0.88$). Preferential crystal orientations ($E \leq 0.06$) are not observed owing to the isotropic shape of the minerals (Table 3). Consequently, the tmt texture does not change from the outermost to innermost portions of the dyke.

Bubbles

Amount and number per area and per volume

The abundances of bubbles determined by 2D and 3D analyses are similar (Fig. 8). DK1 shows a minimum discrepancy of $\sim 1\%$. DK2, DK3, DK6, and DK7 show moderate differences, lower than $\sim 3\%$. Conversely, discrepancies up to $\sim 12\%$ and 6% are observed for DK4 and DK5, respectively (Tables 1 and 2, Fig. 8) and can be ascribed to the heterogeneous distribution of bubbles

in the different portions of the samples (Figs 4 and 9; Supplementary Data Figs S4 and S5). The X-ray μ CT analysis was in fact focused mostly on the volumetric portions of DK4 and DK5 that are enriched in bubbles, whereas the 2D data from thin sections refer to bubble-rich and bubble-poor areas (Fig. 4; Supplementary Data Fig. S4 and S5). This interpretation is corroborated by the very close values observed for 2D (11.2 area %) and 3D data (10.9 vol. %) measured for the most homogeneous sample DK1, showing a high number of small bubbles at the scale of several 10^2 mm^2 and 10^3 mm^3 (Tables 1 and 3). In contrast, DK4 is strongly heterogeneous in terms of the distribution and size of bubbles, with the coexistence of bubble-rich and bubble-poor areas of the order of several 10^3 mm^2 (Figs 4 and 9; Supplementary Data Fig. S4). A similar conclusion holds for the number of bubbles per area and per volume determined from dyke rim to core (Figs 5b and 7b).

Size and shape

The majority of bubbles have lengths of several millimetres, with the exception of DK1, which contains bubbles invariably $<1\text{--}2 \text{ mm}$ (Fig. 4; Supplementary Data Fig. S1–S7). On average, 2D projected equal-area ellipses of a random distributed population of objects

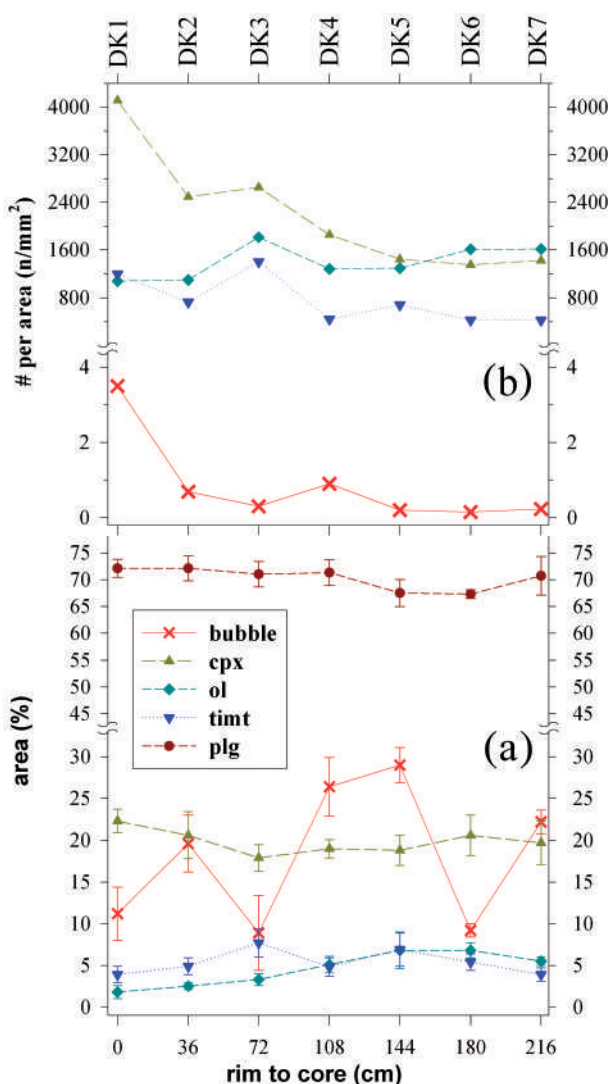


Fig. 5. Quantitative 2D textural features of DK rocks from rim to core. (a) Abundance of bubbles, plg, cpx, ol and timt calculated on a vesicle-free basis; (b) number of single bubbles or minerals per unit area (no. mm^{-2}).

correspond to the intermediate and short sizes of 3D equant to prismatic solids, in agreement with stereology (Higgins, 2000, 2006). Following Higgins (2000), the mode of ratios of short and long axes of equal-area ellipses should be close to the ratio of the actual short (S) and intermediate (I) 3D solids, whereas the 3D long (L) size can be computed using the statistical parameters of such a distribution. Unfortunately, this stereological approach yielded inaccurate values for the S , I and L bubbles. Therefore, we decided to use ratios of the axes of 2D equal-area ellipses, according to the model proposed by Morgan & Jerram (2006), which also provides confidence of the attained results. The computed 3D axes from 2D ellipses of bubbles are shown in Fig. 10. With the exception of DK6, the samples provide moderate to highly accurate results. DK1, DK2 and DK3 correspond to ellipses with 3D axes close to 1:0.4/

0.3:0.3/0.2, whereas DK4, DK5 and DK7 approximate to 1:0.9/0.7:0.7/0.6 (Fig. 10).

Within the limits of the selected spatial resolution (of the order of $10\ \mu\text{m}$) X-ray μCT reveals that DK7 and DK1 have the largest ($0.22\ \text{mm}^3$) and smallest ($0.002\ \text{mm}^3$) bubble volumes, respectively. The other samples show variable bubble volumes of the order of 10^{-1} or $10^{-2}\ \text{mm}^3$. The maximum length measures the longest segment passing from the centre of mass of each bubble. The actual 3D maximum and minimum lengths are invariably lower than 1–2 mm and higher than 0.02 mm for DK1 and DK5 (Fig. 11). For these samples, bubbles with maximum length sizes $<0.1\ \text{mm}$ were not detected by the 2D data (see above). The other DK samples have maximum lengths ranging from 0.05 mm up to several millimetres (Fig. 11). The sphericity describes the largest luminous sphere inscribed in a bubble. It is noteworthy that sphericity does not discriminate prolate ($L \gg I \sim S$) from oblate ($L \sim I \gg S$) bubbles. The 3D quantified sphericity ranges between 0.2 and 1, but frequently it is higher than 0.5 (Fig. 11). Diagrammatically, the sphericity of bubbles appears to crudely decrease as a function of the maximum length, but there is no analytical correlation between these parameters (Fig. 11). Furthermore, the maximum length and sphericity of bubbles do not follow any specific trend within a single DK sample, or from DK1 to DK7 (Fig. 11). The variation of bubble shape as a function of size (as obtained by X-ray μCT) indicates that a significant number of small bubbles (especially in DK1 and DK5) are undetected by 2D image analysis. At the same time, bubbles with an extreme low sphericity, such as tubular or extremely stretched ones, are never recognized in 3D (Fig. 11) or 2D images (Fig. 4; Supplementary Data Fig. S1–S7).

Distribution and orientation

The isotropy (I) and elongation (E) indices, evidencing the tendency to develop (or not) a fabric (Table 3), were extracted considering only the bubbles not touching the edges of the VOIs; that is, those preserving their real shape and volume. The index I represents the similarity of a fabric to a uniform distribution (Benn, 1994). In dyke samples, bubbles exhibit a high isotropic distribution ($I=0.70\text{--}0.78$) (Table 3), in agreement with the presence of bubble-rich and bubble-poor areas (Fig. 4; Supplementary Data Fig. S1–S7). The preferred orientation of bubbles is quantified by the elongation, which is invariably low ($E=0.03\text{--}0.10$), from dyke rim to core. This is apparently in contrast to some 2D images (Fig. 4; Supplementary Data Fig. S1–S7), where bubbles may appear arranged along several preferred directions. However, 2D bubble orientations are sub-fabrics only in thin rock portions, and disappear in a 3D rock volume. This finding suggests that, in the case of DK samples, 3D upshots represent the best method to outline the lack of a homogeneous bubble distribution and preferential bubble alignments.

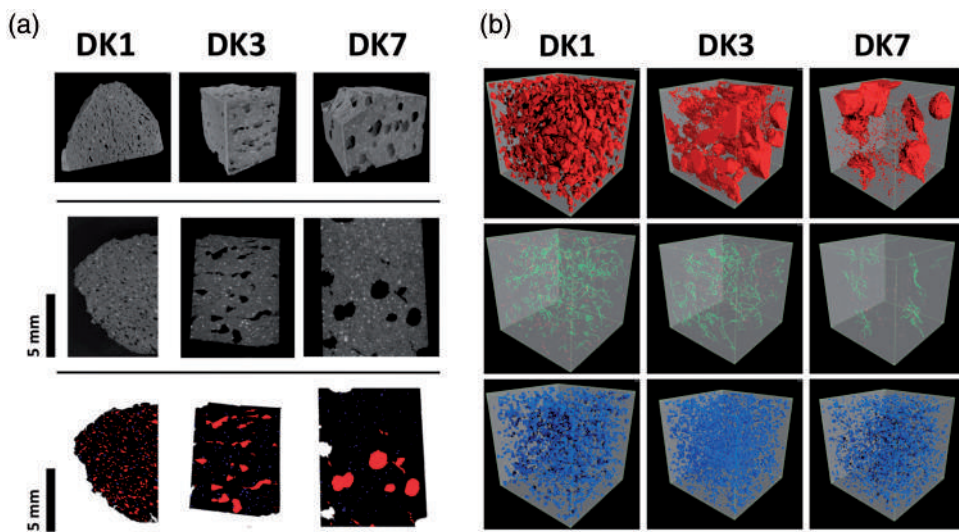


Fig. 6. (a) Top row: renderings of the imaged volumes for the investigated samples. Middle row: reconstructed axial slices. Bottom row: the same slices as reported in the middle row where bubbles (red) and tmt (blue) not connected with the borders have been segmented. (b) Renderings of $500 \times 500 \times 500$ voxels sub-volumes of selected samples. Top row: isosurface renderings of the bubble phase. Middle row: skeletons of the bubble network (green, node-to-node connections; red, end-to-end branches). Bottom row: isosurface rendering of the tmt phase.

Connection and coalescence

The connectivity density (CD) is a proxy for determining the amount of connected and unconnected bubbles in dyke samples. DK1 shows the lowest CD value (Table 3), in agreement with the highest amount of unconnected channels (Fig. 11). However, for all the samples, the CD is always near zero, indicating that bubbles are scarcely connected. Bubbles are not perfectly equally distributed within the rocks, allowing us to identify different sub-volumes for each VOI and to perform LKC skeletonization. The minimum (-10.4) and maximum (1.7) values of connectivity density are obtained for sub-volumes from DK1 and DK5, respectively. This suggests that, with respect to the dyke margin (DK1), the scarce amounts of connected bubbles in the inner portions of the dyke (from DK2 to DK7) were formed at an early stage of the magmatic intrusion. Moreover, coalescence attributes were estimated by the integral of the mean curvature (M_V), resolving the dominance of convex or concave structures. Positive M_V values for all the samples indicate the dominance of convex surfaces owing to the abundance of isolated bubbles, especially in DK1, which shows the highest number of bubbles (Table 3).

DISCUSSION

The 2D and 3D data for bubbles allow us to reconstruct the solidification and emplacement conditions of the dyke, in concert with fluid-dynamics effects. DK1 is radically different from the other dyke samples, owing to the fact that it contains a great number of small bubbles, whereas large bubbles are virtually absent. This indicates that, at the early stage of solidification, a significant rapid cooling rate developed only at the contact

with the country-rocks (in a layer a few decimetres thick; Mollo *et al.*, 2011). At the same time, it is important to stress that the amount of bubbles is between 10 and 30 area % (and/or vol. %), whereas the textures of minerals are variable (Table 1, Figs 5 and 7). High degrees of bubble deformation and textural change are not observed from dyke rim to core (Figs 6, 10 and 11). Obviously, most of the bubbles nucleated before the mineral phases, to grow partially in parallel with the crystals.

Solidification process

Minerals show only minor variations of their textural attributes in concert with moderate and almost linear changes in the composition of plg, cpx, and tmt from DK1 to DK7 (Fig. 1; Mollo *et al.*, 2011; Scarlato *et al.*, 2014). Conversely, the abundance of plg and cpx, as well as the number per area of cpx do not change linearly (Tables 1 and 3; Figs 4–7; Supplementary Data Fig. S1–S7). The texture of the crystalline phases strongly contrasts with irregular variations in the amount, size, shape, distribution, and orientation of bubbles (Tables 1 and 3; Figs 4–7, 10 and 11; Supplementary Data Fig. S1–S7). In the shallow portions of the Mt Etna feeding system, H_2O strongly controls magma solidification and rheology (Mollo *et al.*, 2015b; Perinelli *et al.*, 2016), being the most important dissolved volatile species and the most abundant gas in bubbles (Del Gaudio *et al.*, 2010; Giacomoni *et al.*, 2014; Fiege *et al.*, 2015; Vetere *et al.*, 2015a). Most of the observed bubbles, especially those of large dimensions, formed before the crystallization of minerals, when the magma was in a liquid state.

The aphyric character of the DK samples, the moderate to small size (<0.2 mm) of crystals, and the high average number of crystals per area or volume suggest an initial crystal-poor magmatic intrusion. Hence the

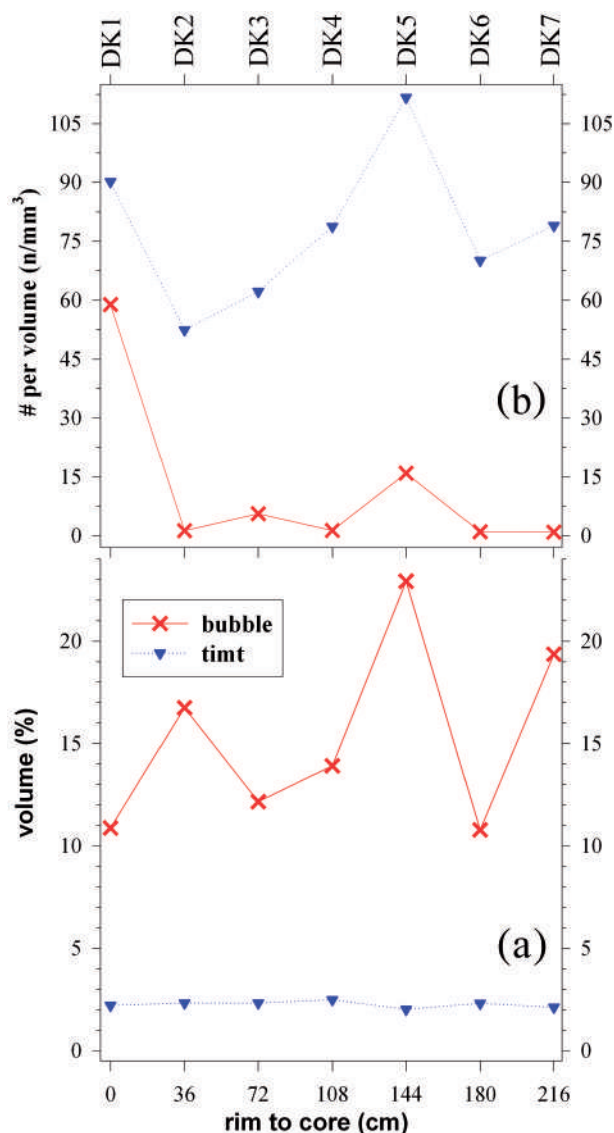


Fig. 7. Quantitative 3D textural features of dyke rocks from rim to core. (a) Abundance of bubbles and timt. (b) Number of bubbles and timt per unit volume (no. mm^{-3}).

magma was injected into the host-rocks under super-heated conditions or close to its liquidus temperature. In turn, crystals mostly nucleated and grew during the ascent of the DK magma by both decompression-induced degassing (Hammer, 2008; Fiege *et al.*, 2015; and references therein) and cooling (Iezzi *et al.*, 2008, 2011; Mollo *et al.*, 2011; Vetere *et al.*, 2013, 2015a) processes. At the time of emplacement, the sampled dyke level was located at 100–300 m depth (Mollo *et al.*, 2011). Indeed, large bubbles nucleated below this level, whereas tiny bubbles resulted from a second minor event of H_2O exsolution (Figs 10 and 11), which occurred close to this shallow level. The volatile liberation also induced the onset of plg and cpx nucleation. All these processes contributed to the rise of the viscosity of the magma, as well as decelerating and/or halting the intrusion. The solubility and exsolution of H_2O are

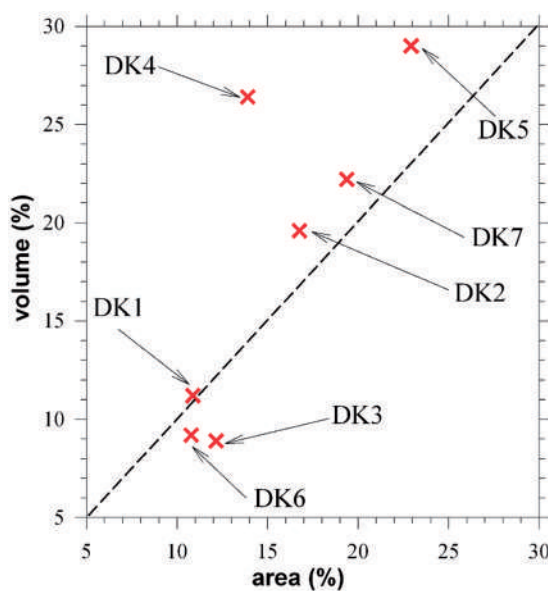


Fig. 8. Abundances of bubbles determined by 2D (area %) and 3D (vol. %) image analyses. The dashed line corresponds to the 1:1 relation.

strongly dependent on pressure, whereas temperature changes control the thermal regimes favouring crystal nucleation and growth (e.g. Hammer, 2008; Iezzi *et al.*, 2008, 2011; Vetere *et al.*, 2013, 2015b; Fiege *et al.*, 2015).

Plg nucleation was initially driven by decompression-induced degassing, at a moderate to high degree of undercooling, forming tiny grains with a high number per area, and frequent self-aggregation of crystals (Figs 4 and 5; Supplementary Data Fig. S1–S7). A similar process holds for cpx. If the initial nucleation of plg and cpx was induced only by cooling, the number of crystals per area should be very high at the dyke rim and progressively decrease towards the core, as expected owing to the effect of a variable cooling rate condition (Cashman, 1992; Hammer, 2008; Vetere *et al.*, 2013, 2015a). The decreasing trends of the number per area of bubbles and cpx, as well as the formation of tiny bubbles in DK1, are indicative of the significant effect of cooling only in proximity of the dyke margin in contact with the host-rock (Figs 4–7).

Fluid-dynamic mechanism

A first important characteristic of the dyke is the irregular distribution of exsolved H_2O (i.e. bubbles). Both 2D and 3D textural and fabric analyses clearly evidence the irregular pattern of bubbles from the dyke rim to the core (Figs 5 and 7). The 2D data reveal variable bubble orientations (especially of the larger ones), whereas the 3D data suggest the absence of preferred bubble orientations. The imaged bubbles, in either two or three dimensions, never show features indicative of a high finite rate of strain, such as high aspect-ratios, tube shapes, extreme stretching, breaking-up, narrow trails and/or right or left shearing. This excludes strain partitioning, recently discovered to occur in SiO_2 -rich

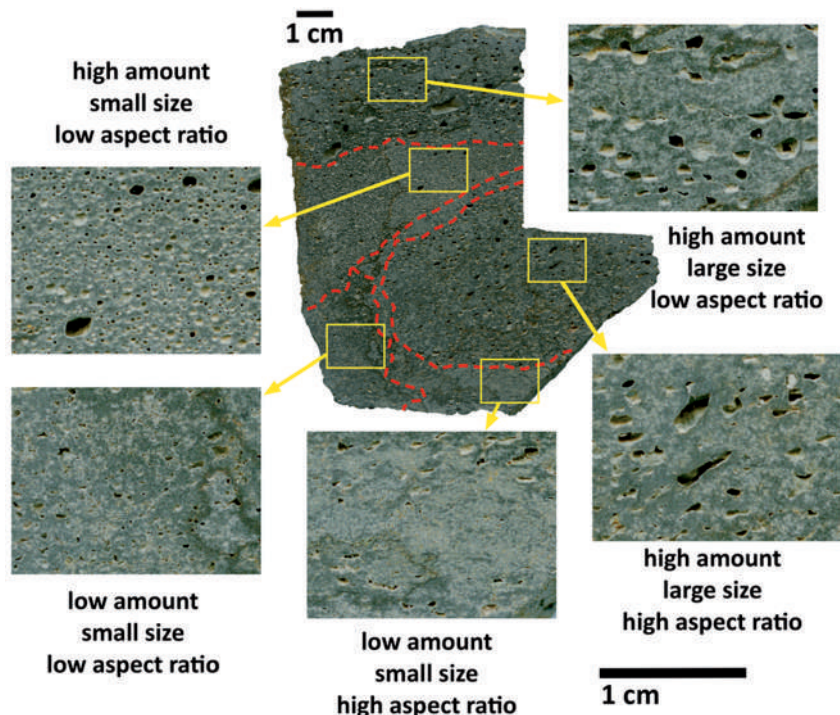


Fig. 9. Surface of the DK4 polished rock with an area of about $8 \times 10^3 \text{ mm}^2$. This shows the coexistence of patches with marked variation in amount, size, and shape (aspect ratio) of bubbles.

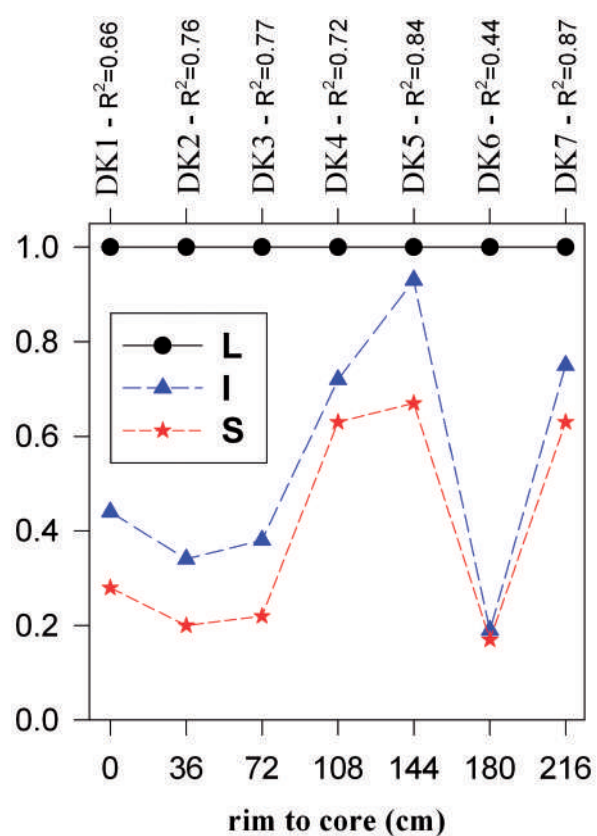


Fig. 10. Variation of the intermediate (I) and short (S) axis ratios normalized to long axis L of bubbles from dyke rim to core. (See text for details)

magmas (Wright & Weinberg, 2009). The size and shape of bubbles do not describe any clear trend from DK1 to DK7 (Figs 10 and 11). In contrast, bubbles are severely stretched at the margins and base of lava flows, developing high strain rates and slightly deformed features in the central and shallower portions (Polacci & Papale, 1997; Polacci *et al.*, 1999; Rust *et al.*, 2003; Clemente *et al.*, 2007). A further significant aspect concerns the fact that all DK samples come from the same depth of magma emplacement; that is, all the rocks solidified at the same pressure along the x direction.

These bubble characteristics can reflect movement and deformation, not only along the vertical direction z but also along x and y, suggesting that the emplacement of magma below and near the DK original level occurred by non-laminar behaviour owing to transitional and/or turbulent regimes. In a laminar flow, the maximum length of bubbles must orient in the direction of transport, translating to the z axis for the studied dyke (Fig. 1). In parallel, the anisotropy of bubbles must increase from the central to outer fluid portions (Gonnerman & Manga, 2012; Manga *et al.*, 2014). These classical features of laminar flows are lacking in the dyke rocks. The textural and fabric characteristics observed for the majority of bubbles can be rationally explained by transitional and/or turbulent fluid conditions.

This conclusion also validates the apparent discrepancies in 2D and 3D bubble contents measured for DK4 (Fig. 9). The polished surface of this sample displays, in

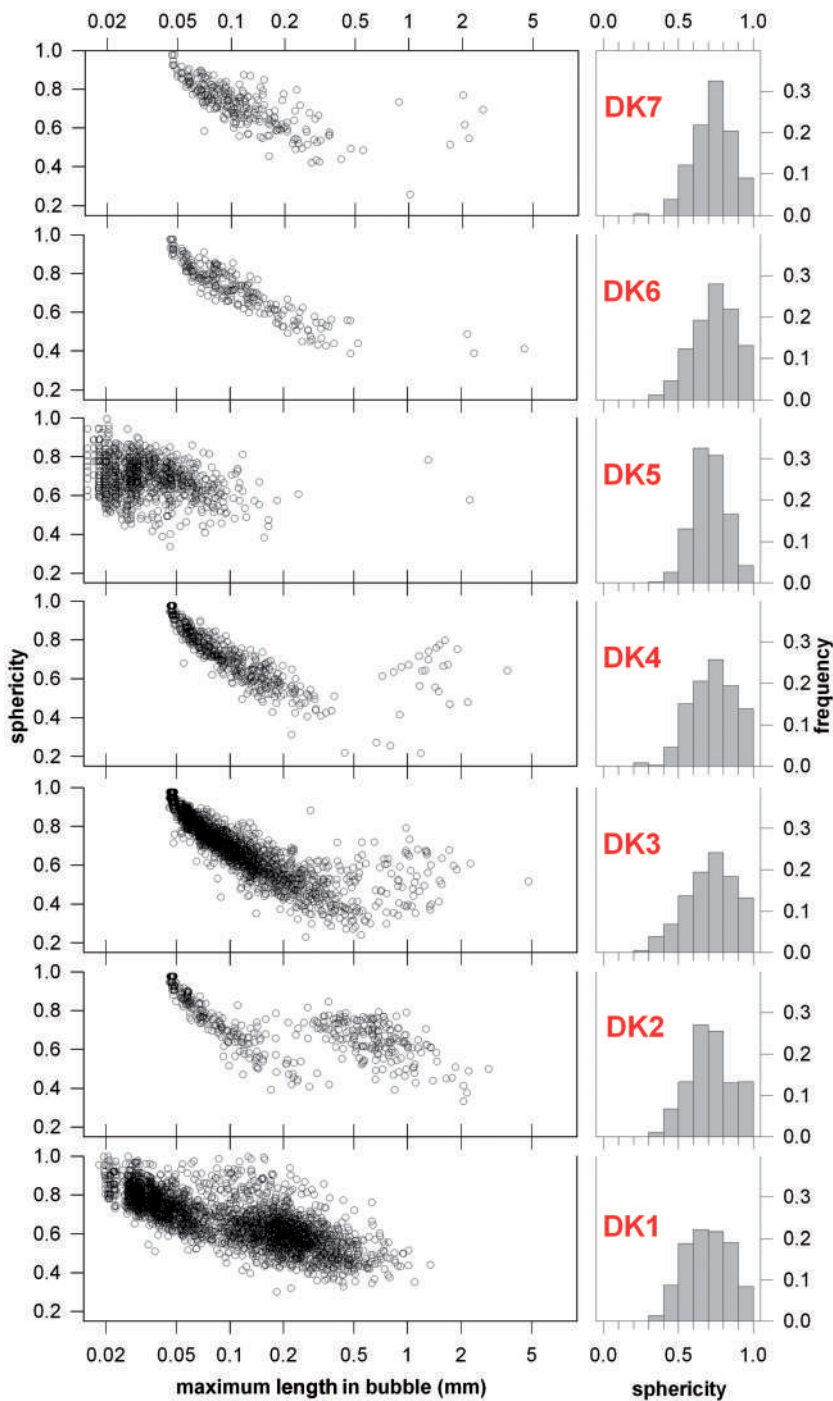


Fig. 11. Maximum length of bubbles vs sphericity (left side) and frequency distribution of sphericity (right side).

an area of only $8 \times 10^3 \text{ mm}^2$, the coexistence of portions with bubbles having highly variable amounts, sizes, and shapes. In this surface, bubble shapes with high and low anisotropy can be explained by localized and variable strain rate; for instance, close to or far from vortices. It is also reasonable that the supposed transient and/or turbulent dynamics were limited or even lacking within a few tens of centimetres from the dyke margin, owing to the major effect of heat transport. The presence of transitional to turbulent regimes also limits

temperature changes along the x and y dyke directions, at least during non-laminar dynamics (Spera, 1980; Huppert & Sparks, 1985; Spence & Turcotte, 1990; Carrigan, 2000).

Physical constraints

Thermometric estimates from dyke core to rim indicate that the early crystallization of plg and cpx occurred at $1119 \pm 19^\circ\text{C}$ and $1126 \pm 26^\circ\text{C}$, respectively (Mollo *et al.*,

2011). These comparable thermal conditions agree with the similar crystal dimensions (<0.2 mm) measured for plg and cpx across the dyke (Fig. 4; Supplementary Data Fig. S1–S7). Furthermore, the total H_2O content dissolved in the magma has been estimated to be 1.6 ± 0.3 wt % at $f\text{O}_2$ of $\text{NNO} + 0.9 \pm 0.9$, where NNO is the nickel–nickel oxide buffer (Mollo *et al.*, 2011). The emplacement pressures have been computed in this study by considering field observations (see the Supplementary Excel spreadsheets). Volcanic rocks at Mt Etna are trachybasalts emitted principally as dense lavas and secondarily as scoriae. We thus considered three densities of 2000, 2500, and 3000 kg m⁻³ to bracket the pressure conditions as a function of depth below the original dyke surface (100–300 m depth):

$$P = \rho \times d \times g$$

where ρ is the density (kg m⁻³) of the overlying rocks or dyke magma, d is the dyke width (x direction in Fig. 1), and g is the acceleration due to gravity (m s⁻²). The calculations envisage a maximum and conservative range of pressures between 2 MPa (ρ of 2000 kg m⁻³ at 100 m) and 9 MPa (ρ of 3000 kg m⁻³ at 300 m) (Fig. 12).

The solubility of water in magma and the volume of exsolved gas phases have been computed using the models of Papale *et al.* (2006) and Solex (Whitam *et al.*, 2012), assuming closed-system conditions. Three initial

H_2O amounts of 0.5, 1, and 2 wt % were considered together with 1000 ppm of CO_2 , 2000 ppm of S and 2000 ppm of Cl, typical for Etnean magmas (Spilliaert *et al.*, 2006; Collins *et al.*, 2009; Lanzafame *et al.*, 2013). The results indicate that 0.5, 1, and 2 wt % H_2O start to exsolve at about 10, 20, and 55 MPa, respectively (Fig. 12).

To evaluate the rheological conditions plausible for dyke solidification and its fluid dynamics, the density change of magma has been simulated in a closed system as a function of P , 1 wt % H_2O , 950–1150°C, and 0–40 wt % plg and 15 wt % cpx. The solubility model of Papale *et al.* (2006) was used to calculate the wt % and mol % of H_2O dissolved and exsolved, whereas the density of magma was calculated using the Conflow program (Mastin, 2002). All these data were used as input parameters for the ideal gas law:

$$V = R \times n \times T / P$$

where V is volume (m³), n is moles (mol %), and R is the universal gas constant (see the Supplementary Excel spreadsheets). At 5.5 and 6.5 MPa, the gas phase is 10–30 vol. %, resembling the total amount of bubbles (Figs 12 and 13). This narrow range of P also corresponds to a rapid change in density, roughly from 1800 and 2400 kg m⁻³. It is worth noting that at $P < 10$ MPa the amount of gas is low or absent and the density of

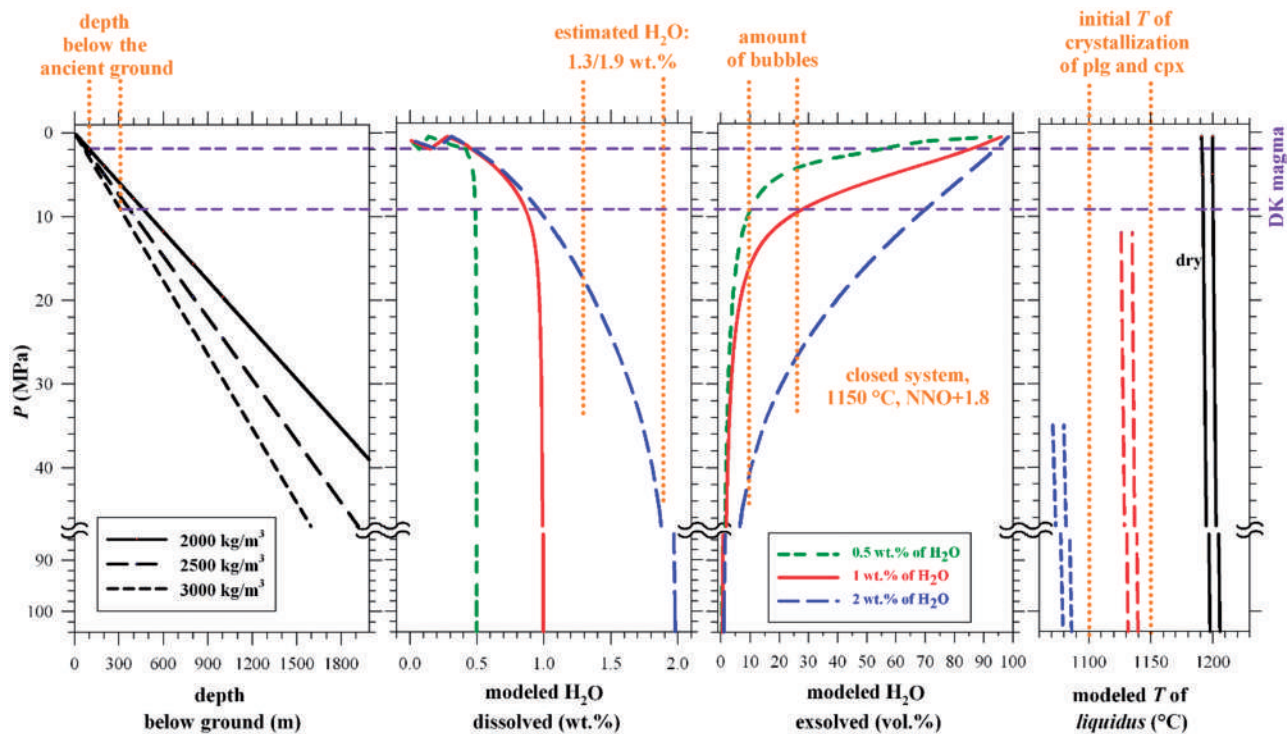


Fig. 12. Variation of physical parameters as a function of P . (Left) Calculated P as a function of estimated 100–300 m thick overlying rocks with variable density (ρ_{rock}). (Intermediate left) Modelled H_2O solubility with SOLEX and H_2O plagioclase saturation estimated with hydrometric model (Mollo *et al.*, 2011). (Intermediate right) Modelled H_2O vol. % exsolution in a closed system, at $T = 1150^\circ\text{C}$ and $\text{NNO} + 1.8$ using SOLEX and the range of measured bubbles (Tables 1 and 3). (Right) Estimated liquidus temperature by MELTS (Papale *et al.*, 2006) between NNO and QFM + 3 (where QFM is quartz–fayalite–magnetite buffer) plus thermal ranges of the onset of crystallization (Mollo *et al.*, 2011). The horizontal violet lines indicate the pressure range for the DK magma at its ancient depth below the ground.

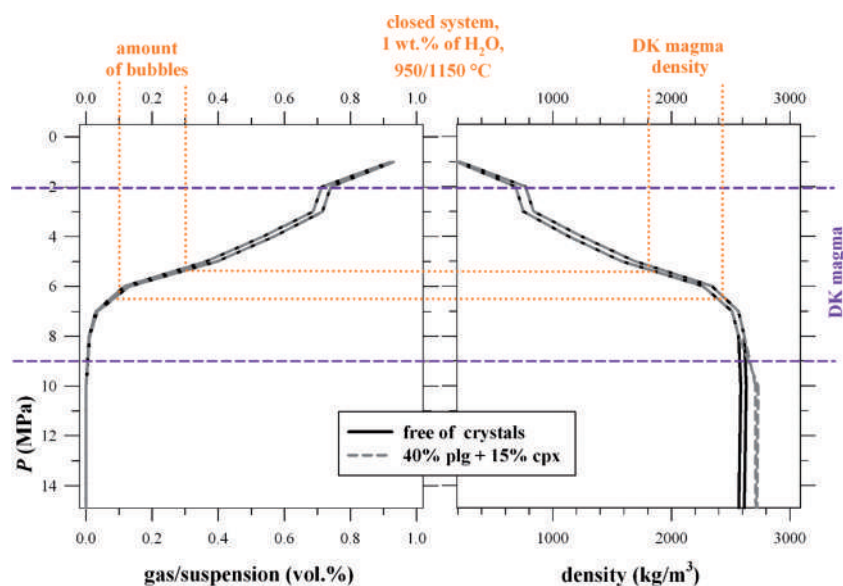


Fig. 13. Simulations of gas vs magmatic suspension ratio (left) and its density at relevant P (0–15 MPa), T (950–1150°C), H_2O (1 wt % assuming a closed system), and amount of crystals (0–55% equals 40 wt % plg + 15 wt % cpx). The simulations were performed using the solubility model of Papale *et al.* (2006), which provides also gas–liquid partitioning and moles of exsolved H_2O . These data were then used in the ideal gas law (see the text and Supplementary Excel spreadsheets). The density of the dyke magma is $\geq 2400 \text{ kg m}^{-3}$ and rapidly decreases to 1800 kg m^{-3} to attain the measured range of bubbles.

the magmatic suspension slightly changes by about 150 kg m^{-3} (the densities of plg, cpx, and melt are 2700, 3250, and 2600 kg m^{-3} , respectively). In general, dykes intruding with a low overpressure can ascend by means of a density contrast between the magma and country-rocks (Carrigan, 2000; Jaupart, 2000; Gonnerman & Taisne, 2015). In the present case, if the magma was injected with a low overpressure, its ascent may be possible only for a wall-rock density $> 2400 \text{ kg m}^{-3}$ (Fig. 13).

A further calculation focused on the liquidus temperature considering 0, 1, and 2 wt % H_2O , up to the limit of pressure required to retain water dissolved in the magma at fO_2 of NNO + 1. This set of numerical results is compared with the saturation temperatures of plg and cpx (Mollo *et al.*, 2011). Under anhydrous conditions the liquidus temperature corresponds to 1190–1200°C, whereas it decreases to 1130 and 1075°C at 1 and 2 wt % H_2O , respectively. The computation with 2 wt % H_2O does not match at all with the saturation temperatures of plg and cpx crystallization (Fig. 12). The computation with 1 wt % H_2O produces up to 30 vol. % at 10–16 MPa, corresponding to a depth of 350–600 m for a 2500 kg m^{-3} density (i.e. below the dyke magma pressure level of 2–9 MPa). Also, 1 wt % H_2O originally dissolved in magma means that 0.25–0.5 wt % H_2O exsolved at pressure ≥ 2 –9 MPa. Thus, the shallow magma contained only 0.5–0.75 wt % H_2O (Fig. 12), in agreement with the water concentration estimated to be in equilibrium with the crystals at the onset of plg and cpx crystallization (Mollo *et al.*, 2011). Up to 30 vol. % of bubbles formed before the magma attained pressures of 2–9 MPa (Fig. 12). In turn, transient to turbulent regimes recorded by most of the bubbles occurred when the magma was at pressures of between 9 and

16 MPa (Fig. 12). A non-laminar dynamic flow probably took place also at $P < 16$ MPa, but it is not detectable owing to the lack of phases at $P \geq 16$ MPa. The computation with 0.5 wt % H_2O produces similar results but at pressures lower than those determined using 1 wt % H_2O .

When the magma attained a pressure level between 2 and 9 MPa, 1 wt % H_2O further exsolved (Fig. 12) accompanied by a temperature decrease owing to the contact with the cold wall-rock. Both decompression and cooling caused rapid and massive crystallization, with formation of new cpx and plg nuclei or overgrowths on early formed crystals by attachment processes (Iezzi *et al.*, 2008, 2011, 2014). All these aspects favoured an abrupt increase of crystals in the magma, decelerating or even arresting the flow. The last step of crystallization occurred at $T < 1100$ °C as recorded by plg and cpx crystal rims (Mollo *et al.*, 2011).

The retrieved magma densities have been used for the calculation of the Reynolds numbers, through the equation

$$\text{Re} = \rho \times d \times v / \eta$$

where ρ is density of the magma between 1800 kg m^{-3} (30 vol. % bubbles) and 2500 kg m^{-3} (free of crystals and with a few bubbles), d is the dyke width, v is the average ascent velocity and η is the melt viscosity. This last parameter was calculated using the equation of Giordano *et al.* (2008) at 0.5 and 1 wt % H_2O and 1000–1200°C, whereas the effect of crystals on viscosity has been modelled using data from Vona *et al.* (2011), considering crystals with a 3:1 aspect ratio and a 0.1 s^{-1} strain rate. The progressive differentiation of the

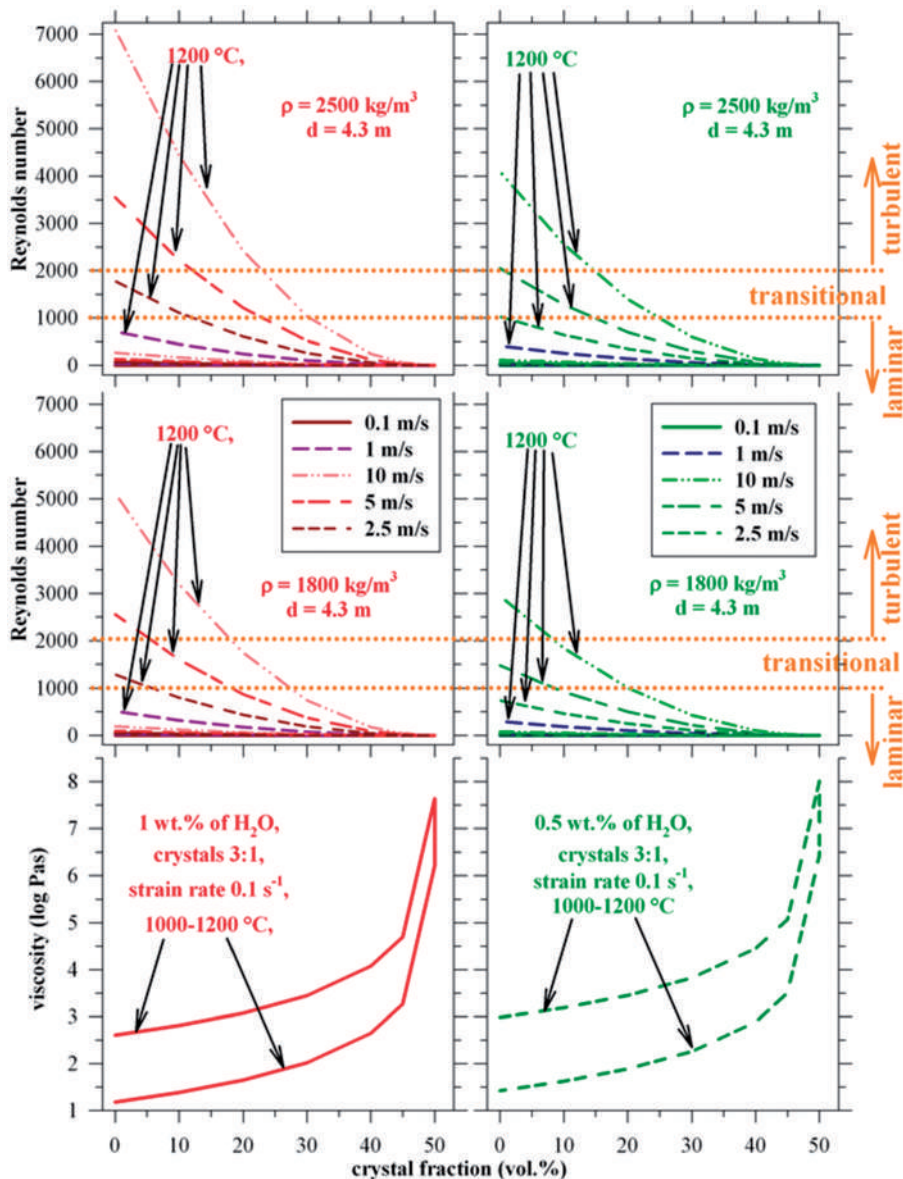


Fig. 14. Bottom: simulations of viscosity for DK magmatic suspension with 1 wt % (left column) and 0.5 wt % (right column) of dissolved water, at 1200 and 1000°C at a moderate strain rate, for crystal contents between 0 and 50 vol. %. These calculated viscosities were used as input data to calculate the Reynolds number (top and middle row) for a dyke width of 4.3 m using two densities (ρ) of 1800 and 2500 kg m^{-3} (from Fig. 13) for four ascent velocities. The simulation path at 1000°C invariably attains a Reynolds number of only some tens to a few hundreds. The end of laminar regime is fixed at 1000, and a full turbulent regime is arbitrarily set above 2000 (see text).

residual melt as a function of crystals and bubbles has not been considered, given that this strategy is clearly conservative owing to the fact that melt viscosity increases with increasing SiO_2 of the melt (Gonnerman & Manga, 2012; Manga *et al.*, 2014). Viscosity paths are very similar, with only a weak downward shift at 0.5 wt % H_2O (Fig. 14). Overall, the viscosity increases by about two orders of magnitude when the crystal content increases from 0 to 40 vol. %, but the most important changes are observed for crystallization up to 50 vol. % (Fig. 14).

These viscosity values were translated to Re numbers at 1800 and 2500 kg m^{-3} , considering five ascent

velocities of 0.1, 1, 2.5, 5, and 10 m s^{-1} (Fig. 14), reproducing the ascent rates estimated for Etnean magmas (Mollo *et al.*, 2015a). Critical Re numbers were set at 1000 and 2000 for shifting from laminar to transitional and from transitional to turbulent regimes, respectively (Huppert & Sparks, 1985; Emerman & Turcotte, 1986; Spence & Turcotte, 1990). Results show that, at $T < 1200^\circ\text{C}$ and density of 1800 kg m^{-3} , an ascent velocity $>2.5 \text{ m s}^{-1}$ is sufficient to pierce the transitional field when the crystal content is <10 vol. % and H_2O is 0.5–1 wt % (Fig. 14). At these conditions, a turbulent regime is triggered for an ascent velocity $>5 \text{ m s}^{-1}$ (Fig. 14). At lower values, non-laminar regimes are

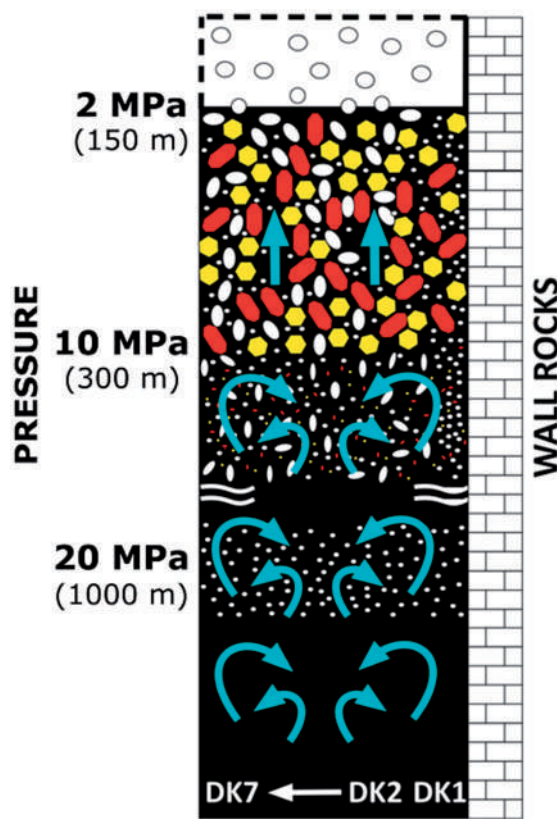


Fig. 15. Schematic illustration summarizing the most important steps that drive dyke emplacement. At $P > 20$ MPa the DK magma is free of crystals and bubbles, containing only 1 wt % of H_2O . A non-laminar fluid flow develops (cyan arrows). Between 20 and 10 MPa, H_2O begins to exsolve, forming up to 30 vol. % of bubbles (tiny circular to large oblate white bubbles) under a transitional to turbulent regime. Decompression-induced degassing leads to the formation of plg and cpx cores (tiny red and yellow crystals). The crystallization reduces the ascent rate of the magma and shifts the flow regime to laminar. Between 9 and 2 MPa, plg and cpx continue to grow under the effect of cooling rate. The crystal size increases to 0.2 mm, halting the flow of magma.

produced when the temperature decreases and the crystal content increases (Figs 13 and 14). These numerical results rationally support the transient and/or turbulent regimes deduced from the textural and fabric characteristics of bubbles (Table 3; Figs 4, 6 and 9; Supplementary Data Fig. S1–S7). The complex history of the dyke magma proposed here has been summarized in Fig. 15, drawing attention to the most important interpreted steps occurred during its emplacement.

CONCLUSIONS

This study deals with the physicochemical conditions driving the solidification of a dyke at Mt Etna volcano. At $P > 10$ MPa, the original magma feeding the intrusion was virtually crystal-free, with a dissolved H_2O content close to 1 wt %; at $P < 10$ MPa, abundant degassing-induced crystallization took place via H_2O exsolution. Crystals continued to grow under the effect of an increasing cooling rate from the innermost dyke portion

to the wall-rocks. The ascent velocity of magma was of the order of a few m s^{-1} , with a transitional to turbulent regime before the growth of minerals. Thus, dyke emplacement occurred at conditions close to the liquidus surface of the magma. Under such circumstances, the transition to turbulent regimes determined a more uniform distribution of the ascent velocity and random variation of the strain rate.

Comparison between the 2D and 3D data for bubbles indicates that common 2D textures give confident quantification of the amount and number per area of bubbles. Conversely, actual bubble orientations are identified only by 3D textures, despite the overall mathematical description of bubble shapes requiring both 2D and 3D quantitative approaches. The occurrence of non-laminar fluid-dynamic regimes is indicated by the following: (1) the presence of bubble-rich, -poor and-free patches with their irregular amounts through the dyke thickness; (2) the absence of any bubble size, shape and fabric relations moving from outer to inner DK portions; (3) the observations of eddies and vortices. Transitional to turbulent regimes have been possibly recorded owing to rapid change in viscosity, which has frozen in the early deformation of bubbles.

Further analysis by phase-contrast synchrotron radiation X-ray microtomography will allow investigation of the 3D morphology and texture of plagioclase, clinopyroxene and olivine phases in the same dyke sample. It can be concluded that similar investigations on Etnan dykes may provide novel insights into the fluid dynamics, transport regimes, and ascent velocities of the magmas, with valuable ramifications for geophysical and hazard modelling.

ACKNOWLEDGEMENTS

The authors are grateful to M. D. Higgins, F. Arzilli and an anonymous reviewer for their valuable comments and suggestions, which improved the clarity and significance of this study. The editor M. Wilson is warmly acknowledged for her editorial handling. The 2D data reported in this study were first collected and treated during the Master's thesis of F.L. at the University G. d'Annunzio. Special thanks go to F. Brun (University of Trieste, Italy) for helpful discussions on the quantitative analysis, and to D. Dreossi and N. Sodini (Elettra-Sincrotrone, Trieste) for their support in performing the experiments.

FUNDING

This work was made possible by the support of the following institutions and programmes: Università G. d'Annunzio – 'Fondi Ateneo' and PRIN project 'Experimental determination of the glass-forming ability, nucleation and crystallization of natural silicate melts' awarded to G.I. Networking support was provided by the EXTREMA COST Action MP1207.

SUPPLEMENTARY DATA

Supplementary data for this paper are available at *Journal of Petrology* online.

REFERENCES

- Acocella, V. & Neri, M. (2009). Dyke propagation in volcanic edifices: Overview and possible developments. *Tectonophysics* **471**, 67–77.
- Al-Raoush, R. & Papadopoulos, A. (2010). Representative elementary volume analysis of porous media using X-ray computed tomography. *Powder Technology* **200**, 69–77.
- Álvarez-Valero, A. M., Okumura, S., Arzilli, F., Borrajo, J., Recio, C., Ban, M., Gonzalo, J. C., Benítez, J. M., Douglas, M., Sasaki, O., Franco, P., Gómez-Barreiro, J. & Carnicer, A. (2016). Tracking bubble evolution inside a silicic dyke. *Lithos* **262**, 668–676.
- Andersson, M., Almqvist, B. S. G., Burchardt, S., Troll, V. R., Malehmir, A., Snowball, I. & Kübler, L. (2016). Magma transport in sheet intrusions of the Alnö carbonatite complex, central Sweden. *Scientific Reports* **6**, 27635.
- Aubourg, C., Tshoso, G., Le Gall, B., Bertrand, C., Tiercelin, J. J., Kampunzu, A. B., Dyment, J. & Modisi, M. (2008). Magma flow revealed by magnetic fabric in the Okavango giant dyke swarm, Karoo igneous province, northern Botswana. *Journal of Volcanology and Geothermal Research* **170**, 247–261.
- Baker, D. R., Brun, F., O'Shaughnessy, C., Mancini, L., Fife, J. L. & Rivers, M. (2012). A four-dimensional X-ray tomographic microscopy study of bubble growth in basaltic foam. *Nature Communications* **3**, 1135.
- Bascou, J., Camps, P. & Dautria, J. M. (2005). Magnetic versus crystallographic fabrics in a basaltic lava flow. *Journal of Volcanology and Geothermal Research* **145**, 119–135.
- Benn, D. I. (1994). Fabric shape and the interpretation of sedimentary fabric data. *Journal of Sedimentary Research* **A64**, 910–915.
- Bjarne, S., Almqvist, G., Bosshard, S. A., Hirt, A. M., Mattsson, H. B. & Hetényi, G. (2012). Internal flow structures in columnar jointed basalt from Hrepphólar, Iceland: II. Magnetic anisotropy and rock magnetic properties. *Bulletin of Volcanology* **74**, 1667–1681.
- Branca, S., Coltelli, M., De Beni, E. & Wijbrans, J. (2008). Geological evolution of Mount Etna volcano (Italy) from earliest products until the first central volcanism (between 500 and 100 ka ago) inferred from geochronological and stratigraphic data. *International Journal of Earth Sciences* **97**, 135–152.
- Bruce, P. M. & Huppert, H. E. (1990). Solidification and melting along dykes by the laminar flow of basaltic magma. In: Ryan, P. (ed.) *Magma Transport and Storage*. John Wiley, pp. 87–102.
- Brun, F., Mancini, L., Kasaei, P., Favretto, S., Dreossi, D. & Tromba, G. (2010). Pore3D: a software library for quantitative analysis of porous media. *Nuclear Instruments and Methods in Physics Research A* **615**, 326–332.
- Brun, F., Kourousias, G., Dreossi, D., Mancini, L. & Tromba, G. (2011). A comparative evaluation of ring artifacts reduction filters for X-ray computed microtomography images. *Proceedings of the International Conference on Image Processing*, ICP 6116535, 405–408.
- Callot, J. P., Geoffroy, L., Aubourg, C., Pozzi, J. P. & Mege, D. (2001). Magma flow directions of shallow dykes from the East Greenland volcanic margin inferred from magnetic fabric studies. *Tectonophysics* **335**, 313–329.
- Calvari, S., Groppelli, G. & Pasquare, G. (1994). Preliminary geological data on the south-western wall of the Valle del Bove, Mt. Etna, Sicily. *Acta Vulcanologica* **5**, 15–30.
- Campbell, I. & Schenk, E. T. (1950). Camptonite dykes near Boulder Dam, Arizona. *American Mineralogist* **35**, 671–692.
- Cañón-Tapia, E. & Chávez-Álvarez, M. J. (2004). Theoretical aspects of particle movement in flowing magma: implications for the anisotropy of magnetic susceptibility of dykes. In: Martín-Hernández, F., Lüneberg, C. M., Aubourg, C. & Jackson, M. (eds) *Magnetic Fabric: Methods and Applications*. Special Publications **238**, 227–249.
- Cañón-Tapia, E. & Herrero-Bervera, E. (2009). Sampling strategies and the anisotropy of magnetic susceptibility of dykes. *Tectonophysics* **466**, 3–17.
- Carrigan, C. R. (2000). Plumbing systems. In: Sigurdsson, H., Houghton, B., Rymer, H., Stix, J. & McNutt, S. (eds) *The Encyclopedia of Volcanoes*, 1st edn. Academic Press, pp. 219–235.
- Carrigan, C. R., Schubert, G. & Eichelberger, J. C. (1992). Thermal and dynamical regimes of single- and two-phase magmatic flow in dykes. *Journal of Geophysical Research* **97**, 17377–17392.
- Cashman, K. V. (1992). Textural constraints on the kinetics of crystallization of igneous rocks. In: Nicholls, J. & Russell, J. K. (eds) *Modern Methods of Igneous Petrology: Understanding Magmatic Processes*. Mineralogical Society of America, Reviews in Mineralogy **24**, 259–314.
- Catalano, S., Torrisi, S. & Ferlito, C. (2004). The relationship between Late Quaternary deformation and volcanism of Mt. Etna (eastern Sicily): new evidence from the sedimentary substratum in the Catania region. *Journal of Volcanology and Geothermal Research* **132**, 311–314.
- Chistyakova, S. Y. & Latypov, R. M. (2009). Two independent processes responsible for compositional zonation in mafic dykes of the Åland–Åboland Dyke Swarm, Kestiö Island, SW Finland. *Lithos* **112**, 382–396.
- Clemente, C. S., Amorós, E. B. & Crespo, M. G. (2007). Dyke intrusion under shear stress: Effects on magnetic and vesicle fabrics in dykes from rift zones of Tenerife (Canary Islands). *Journal of Structural Geology* **29**, 1931–1942.
- Collins, S. J., Pyle, D. M. & MacLennan, J. (2009). Melt inclusions track pre-eruption storage and dehydration of magmas at Etna. *Geology* **6**, 571–574.
- Coltellini, M., Garduño, V. H., Neri, M., Pasquare, G. & Pompilio, M. (1994). Geology of the northern wall of the Valle del Bove, Mt. Etna (Sicily). *Acta Vulcanologica* **5**, 55–68.
- Cristofolini, R., Lentini, F., Patanè, G. & Rasà, R. (1979). Integrazione di dati geologici, geofisici e petrologici per la stesura di un profilo crostale in corrispondenza dell'Etna. *Bollettino della Società Geologica Italiana* **98**, 239–247.
- Daniels, K. A., Kavanagh, J. L., Menand, T. & Sparks, R. S. J. (2012). The shapes of dykes: Evidence for the influence of cooling and inelastic deformation. *Geological Society of America Bulletin* **124**, 1102–1112.
- Daniels, K. A., Bastow, I. D., Keir, D., Sparks, R. S. J. & Menand, T. (2014). Thermal models of dyke intrusion during development of continent-ocean transition. *Earth and Planetary Science Letters* **385**, 145–153.
- De Beni, E., Wijbrans, J. R., Branca, S., Coltelli, M. & Groppelli, G. (2005). New results of $^{40}\text{Ar}/^{39}\text{Ar}$ dating constrain the timing of transition from fissure-type to central volcanism at Mount Etna (Italy). *Terra Nova* **17**, 292–298.
- Delaney, P. T., Pollard, D. D., Ziony, J. I. & McKee, E. H. (1986). Field relations between dykes and joints: Emplacement processes and paleostress analysis. *Journal of Geophysical Research* **91**, 4920–4938.

- Del Gaudio, P., Mollo, S., Ventura, G., Iezzi, G., Taddeucci, J. & Cavallo, A. (2010). Cooling rate-induced differentiation in anhydrous and hydrous basalts at 500MPa: Implications for the storage and transport of magmas in dykes. *Chemical Geology* **270**, 164–178.
- D'Orazio, M., Tonarini, S., Innocenti, F. & Pompilio, M. (1997). Northern Valle del Bove volcanic succession (Mt. Etna, Sicily): petrography, geochemistry and Sr–Nd isotope data. *Acta Vulcanologica* **9**, 73–86.
- Elettra (2009). PORE3D—A software library for quantitative analysis on porous media. Elettra, <http://www.elettra.eu/pore3D>.
- Emerman, S. H. & Turcotte, D. L. (1986). Transport of magma and hydrothermal solutions by laminar and turbulent fluid fracture. *Physics of the Earth and Planetary Interiors* **41**, 249–259.
- Eriksson, P. I., Riishuus, M. S., Sigmundsson, F. & Elming, S. A. (2011). Magma flow directions inferred from field evidence and magnetic fabric studies of the Streitishvarf composite dyke in east Iceland. *Journal of Volcanology and Geothermal Research* **206**, 30–45.
- Ernst, R. E. & Baragar, W. R. A. (1992). Evidence from magnetic fabric for the flow pattern of magma in the Mackenzie giant radiating dyke swarm. *Nature* **356**, 511–513.
- Feldkamp, L. A., Davis, L. C. & Kress, J. W. (1984). Practical cone-beam algorithm. *Journal of the Optical Society of America* **A1**, 612–619.
- Femenias, O., Diot, H., Berza, T., Gauffrard, A. & Demaiffe, D. (2004). Asymmetrical to symmetrical magnetic fabric of dykes: Paleo-flow orientations and paleo-stresses recorded on feeder-bodies from the Motru Dyke Swarm (Romania). *Journal of Structural Geology* **26**, 1401–1418.
- Ferlito, C. & Cristofolini, R. (1989). Geologia dell'area sommitale dell'Etna. *Bollettino dell'Accademia Gioenia di Scienze Naturali di Catania* **22**, 357–380.
- Ferlito, C. & Lanzafame, G. (2010). The role of supercritical fluids in the potassium enrichment of magmas at Mount Etna volcano (Italy). *Lithos* **119**, 642–650.
- Ferlito, C. & Nicotra, E. (2010). The dyke swarm of Mount Calanna (Etna, Italy): an example of the uppermost portion of a volcanic plumbing system. *Bulletin of Volcanology* **72**, 1191–1207.
- Ferlito, C., Coltorti, M., Lanzafame, G. & Giacomoni, P. P. (2014). The volatile flushing triggers eruptions at open conduit volcanoes: Evidence from Mount Etna volcano (Italy). *Lithos* **184**, 447–455.
- Fiege, A., Vetere, F., Iezzi, G., Simon, A. & Holt, F. (2015). The roles of decompression rate and volatiles ($H_2O \pm Cl \pm CO_2 \pm S$) on crystallization in (trachy-) basaltic magma. *Chemical Geology* **411**, 310–322.
- Galindo, I. & Gudmundsson, A. (2012). Basaltic feeder dykes in rift zones: geometry, emplacement, and effusion rates. *Natural Hazards and Earth System Sciences* **12**, 3683–3700.
- Geshi, N. & Neri, M. (2011). Dynamic feeder dyke systems in basaltic volcanoes: the exceptional example of the 1809 Etna eruption (Italy). *Frontiers in Earth Science* **2**, 1–11.
- Giacomoni, P. P., Ferlito, C., Coltorti, M., Bonadiman, C. & Lanzafame, G. (2014). Plagioclase as archive of magma ascent dynamics on 'open conduit' volcanoes: the 2001–2006 eruptive period at Mt. Etna. *Earth-Science Reviews* **138**, 371–393.
- Gillot, P. Y., Kieffer, G. & Romano, R. (1994). The evolution of Mount Etna in the light of potassium–argon dating. *Acta Vulcanologica* **5**, 81–87.
- Giordano, D., Russell, J. K. & Dingwell, D. B. (2008). Viscosity of magmatic liquids: a model. *Earth and Planetary Science Letters* **271**, 123–134.
- Gitman, I. M., Askes, H. & Sluys, L. J. (2007). Representative volume: Existence and size determination. *Engineering Fracture Mechanics* **74**, 2518–2534.
- Gonnermann, H. M. & Manga, M. (2012). Dynamics of magma ascent in the volcanic conduit. In: Fagents, S. A., Gregg, T. K. P. & Lopes, R. M. C. (eds) *Modeling Volcanic Processes: The Physics and Mathematics of Volcanism*. Cambridge University Press, pp. 55–84.
- Gonnermann, H. & Taisne, B. (2015). Magma transport in dykes. In: Sigurdsson, H., Houghton, B., McNutt, S., Rymer, H. & Stix, J. (eds) *The Encyclopedia of Volcanoes*, 2nd edn. Academic Press, pp. 215–224.
- Gray, N. H. (1970). Crystal growth and nucleation in two large diabase dykes. *Canadian Journal of Earth Sciences* **7**, 366–375.
- Gray, N. H. (1978). Crystal growth and nucleation in flash-injected diabase dykes. *Canadian Journal of Earth Sciences* **15**, 1904–1923.
- Gudmundsson, A. (2006). How local stresses control magma-chamber ruptures, dyke injections, and eruptions in composite volcanoes. *Earth-Science Reviews* **79**, 1–31.
- Gudmundsson, A., Marinoni, L. B. & Marti, J. (1999). Injection and arrest of dykes: implications for volcanic hazards. *Journal of Volcanology and Geothermal Research* **88**, 1–13.
- Hammer, J. E. (2008). Experimental studies of the kinetics and energetics of magma crystallization. In: Putirka, K. D. & Tepley, F. J. (eds) *Minerals, Inclusions and Volcanic Processes*. Mineralogical Society of America and Geochemical Society, *Reviews in Mineralogy and Geochemistry* **69**, 9–59.
- Hastie, W. H., Aubourg, C. & Watkeys, M. K. (2011). When an 'inverse' fabric is not inverse: an integrated AMS-SPO study in MORB-like dykes. *Terra Nova* **23**, 49–55.
- Hastie, W. H., Watkeys, M. K. & Aubourg, C. (2013). Characterisation of grain-size, shape and orientation of plagioclase in the Rooi Rand dyke swarm, South Africa. *Tectonophysics* **583**, 145–157.
- Herrero-Bervera, E., Walker, G. P. L., Cañón-Tapia, E. & García, M. O. (2001). Magnetic fabric and inferred flow direction of dykes, conesheets and sill swarms, Isle of Skye, Scotland. *Journal of Volcanology and Geothermal Research* **106**, 195–210.
- Higgins, M. D. (2000). Measurement of crystal size distributions. *American Mineralogist* **85**, 1105–1116.
- Higgins, M. D. (2006). Quantitative textural measurements. In: *Igneous and Metamorphic Petrology*. Cambridge University Press, pp. 277; doi: 10.1017/CBO9780511535574.
- Hildebrand, T. & Rüegsegger, P. (1997). A new method for the model-independent assessment of thickness in three-dimensional images. *Journal of Microscopy* **185**, 67–75.
- Holmes, A. & Larwood, H. F. (1929). The tholeiite dykes of the north of England. *Mineralogical Magazine* **22**, 1–52.
- Howard, M. P. (1980). The analysis of flow profiles in a basaltic dyke using strained vesicles. *Journal of the Geological Society, London* **137**, 605–615.
- Huppert, H. E. & Sparks, R. S. J. (1985). Cooling and contamination of mafic and ultramafic magmas during ascent through continental crust. *Earth and Planetary Science Letters* **74**, 371–386.
- Iezzi, G. & Ventura, G. (2002). Crystal fabric evolution in lava flows: results from numerical simulations. *Earth and Planetary Science Letters* **200**, 33–46.
- Iezzi, G., Mollo, S., Ventura, G., Cavallo, A. & Romano, C. (2008). Experimental solidification of anhydrous latitic and trachytic melts at different cooling rates: the role of nucleation kinetics. *Chemical Geology* **253**, 91–101.

- Iezzi, G., Mollo, S., Torresi, G., Ventura, G., Cavallo, A. & Scarlato, P. (2011). Experimental solidification of an andesitic melt by cooling. *Chemical Geology* **283**, 261–273.
- Iezzi, G., Mollo, S., Shahini, E., Cavallo, A. & Scarlato, P. (2014). The cooling kinetics of plagioclase feldspar as revealed by electron-microprobe mapping. *American Mineralogist* **99**, 898–907.
- Ikeda, Y. (1977). Grain size of plagioclase of the basaltic andesite dykes, Iritono, central Abukuma plateau. *Canadian Journal of Earth Sciences* **14**, 1860–1866.
- Jaupart, C. (2000). Magma ascent at shallow levels. In: Sigurdsson, H., Houghton, B., Rymer, H., Stix, J. & McNutt, S. (eds) *The Encyclopedia of Volcanoes*, 1st edn. Academic Press, pp. 237–245.
- Kille, I. C., Thompson, R. N., Morrison, M. A. & Thompson, R. F. (1986). Field evidence for turbulence during flow of basalt magma through conduits from southwest Mull. *Geological Magazine* **123**, 693–697.
- Kitchen, M. J., Pavlov, K. M., Siu, K. K. W., Menk, R. H., Tromba, G. & Lewis, R. A. (2007). Analyser-based phase contrast image reconstruction using geometrical optics. *Physics in Medicine and Biology* **52**, 14.
- Komar, P. D. (1972). Flow differentiation in igneous dykes and sills: profiles of velocity and phenocryst concentration. *Geological Society of America Bulletin* **83**, 3443–3448.
- Komar, P. D. (1976). Phenocryst interactions and the velocity profile of magma flowing through dykes or sills. *Geological Society of America Bulletin* **87**, 1336–1342.
- Lanzafame, G. & Vestch, P. (1985). Les dykes de la Valle del Bove (Etna, Sicile) et le champ de contraintes régionales. *Revue de Géographie Physique et de Géologie Dynamique* **26**, 147–156.
- Lanzafame, G., Mollo, S., Iezzi, G., Ferlito, C. & Ventura, G. (2013). Unraveling the solidification path of pahoehoe 'cicirara' lava from Mount Etna volcano. *Bulletin of Volcanology* **75**, 703–719.
- Lee, T. C., Kashyap, R. L. & Chu, C. N. (1994). Building skeleton models via 3D medial surface axis thinning algorithms. *CVGIP: Graphical Models and Image Proceedings* **56**, 462–478.
- Lindquist, W. B. & Lee, S. M. (1996). Medial axis analysis of void structure in three-dimensional tomographic images of porous media. *Journal of Geophysical Research* **101**, 8297–8310.
- Lister, J. R. & Kerr, R. C. (1991). Fluid mechanical models of crack propagation and their application to magma transport in dykes. *Journal of Geophysical Research* **96**, 10049–10077.
- Maccaferri, F., Bonafede, M. & Rivalta, E. (2011). A quantitative study of the mechanisms governing dyke propagation, dyke arrest and sill formation. *Journal of Volcanology and Geothermal Research* **208**, 39–50.
- Maimon, O., Lyakhovsky, V., Melnik, O. & Navon, O. (2012). The propagation of a dyke driven by gas-saturated magma. *Geophysical Journal International* **189**, 956–966.
- Mancini, L., Dreossi, D., Fava, C., Sodini, N., Tromba, G., Faretto, S. & Montanari, F. (2007). TOMOLAB: The new X-ray microtomography facility @ ELETTRA. *Elettra Highlights 2006–2007*, pp. 128–129.
- Mangan, M. T., Cashman, K. V. & Swanson, D. A. (2014). The dynamics of Hawaiian-style eruptions: a century of study. In: Poland, M. P., Takahashi, T. J. & Landowski, C. M. (eds) *Characteristics of Hawaiian Volcanoes*. US Geological Survey, Professional Papers **1801**, 323–354.
- Mastin, L. G. (2002). Insights into volcanic conduit flow from an open-source numerical model. *Geochemistry, Geophysics, Geosystems* **3**, 1–18.
- McGuire, W. J. (1982). Evolution of the Etna volcano: information from the southern wall of the Valle del Bove caldera. *Journal of Volcanology and Geothermal Research* **13**, 241–271.
- McLeod, P. & Tait, S. (1999). The growth of dykes from magma chambers. *Journal of Volcanology and Geothermal Research* **92**, 231–245.
- Menand, T. & Tait, S. R. (2001). A phenomenological model for precursor volcanic eruptions. *Nature* **411**, 678–680.
- Mollo, S., Lanzafame, G., Masotta, M., Iezzi, G., Ferlito, C. & Scarlato, P. (2011). Cooling history of a dyke as revealed by mineral chemistry: a case study from Mt. Etna volcano. *Chemical Geology* **288**, 39–52.
- Mollo, S., Misiti, V., Scarlato, P. & Soligo, M. (2012). The role of cooling rate in the origin of high temperature phases at the chilled margin of magmatic intrusions. *Chemical Geology* **322–323**, 28–46.
- Mollo, S., Putirka, K., Iezzi, G. & Scarlato, P. (2013). The control of cooling rate on titanomagnetite composition: implications for a geospeedometry model applicable to alkaline rocks from Mt. Etna volcano. *Contributions to Mineralogy and Petrology* **165**, 457–475.
- Mollo, S., Giacomoni, P. P., Andronico, D. & Scarlato, P. (2015a). Clinopyroxene and titanomagnetite cation redistributions at Mt. Etna volcano (Sicily, Italy): Footprints of the final solidification history of lava fountains and lava flows. *Chemical Geology* **406**, 45–54.
- Mollo, S., Giacomoni, P. P., Coltorti, M., Ferlito, C., Iezzi, G. & Scarlato, P. (2015b). Reconstruction of magmatic variables governing recent Etnean eruptions: constraints from mineral chemistry and P - T - fO_2 - H_2O modelling. *Lithos* **212–215**, 311–320.
- Monaco, C., Tapponier, P., Tortorici, L. & Gillot, P. Y. (1997). Late Quaternary slip rates on the Acireale–Piedimonte normal faults and tectonic origin of Mt. Etna (Sicily). *Earth and Planetary Science Letters* **147**, 125–139.
- Monaco, C., Catalano, S., Cocina, O., De Guidi, G., Ferlito, C., Gresta, S., Musumeci, C. & Tortorici, L. (2005). Tectonic control on the eruptive dynamics at Mt. Etna volcano (Sicily) during the 2001 and 2002–2003 eruptions. *Journal of Volcanology and Geothermal Research* **144**, 211–233.
- Monaco, C., De Guidi, G. & Ferlito, C. (2010). The morphotectonic map of Mt. Etna. *Bollettino della Società Geologica Italiana* **129**, 408–428.
- Morgan, D. J. & Jerram, D. A. (2006). On estimating crystal shape for crystal size distribution analysis. *Journal of Volcanology and Geothermal Research* **154**, 1–7.
- Nkono, C., Féménias, O., Diot, H., Berza, T. & Demaiffe, D. (2006). Flowage differentiation in an andesitic dyke of the Motru Dyke Swarm (Southern Carpathians, Romania) inferred from AMS, CSD and geochemistry. *Journal of Volcanology and Geothermal Research* **154**, 201–221.
- Odgaard, A. & Gundersen, H. I. G. (1993). Quantification of connectivity in cancellous bone, with special emphasis on 3D reconstructions. *Bone* **14**, 173–182.
- Ohser, J. & Mücklich, F. (2000). Statistical analysis of microstructure in material science. In: Barnett, V. (ed.) *Statistics in Practice*. John Wiley, 381 pp.
- Otsu, N. (1979). A threshold selection method from gray-level histograms. *IEEE Transactions on Systems, Man and Cybernetics* **9**, 62–66.
- Papale, P., Moretti, R. & Barbato, D. (2006). The compositional dependence of the saturation surface of $H_2O + CO_2$ fluids in silicate melts. *Chemical Geology* **229**, 78–95.
- Perinelli, C., Mollo, S., Gaeta, M., De Cristofaro, S. P., Palladino, D. M., Armienti, P., Scarlato, P. & Putirka, K. D. (2016). An improved clinopyroxene-based hygrometer for Etnean

- magmas and implications for eruption triggering mechanisms. *American Mineralogist* **101**, 2774–2777.
- Pinel, V. & Jaupart, C. (2004). Magma storage and horizontal dyke injection beneath a volcanic edifice. *Earth and Planetary Science Letters* **221**, 245–262.
- Philpotts, A. R. & Philpotts, D. E. (2007). Upward and downward flow in a camptonite dyke as recorded by deformed vesicles and the anisotropy of magnetic susceptibility (AMS). *Journal of Volcanology and Geothermal Research* **161**, 81–94.
- Polacci, M. & Papale, P. (1997). The evolution of lava flows from ephemeral vents at Mount Etna: insights from vesicle distribution and morphological studies. *Journal of Volcanology and Geothermal Research* **76**, 1–17.
- Polacci, M., Cashman, K. V. & Kauahikaua, J. P. (1999). Textural characterization of the pahoehoe–ʻāā transition in Hawaiian basalt. *Bulletin of Volcanology* **60**, 595–609.
- Polacci, M., Baker, D. R., Mancini, L., Favretto, S. & Hill, R. J. (2009). Vesiculation in magmas from Stromboli and implications for normal Strombolian activity and paroxysmal explosions in basaltic systems. *Journal of Geophysical Research: Solid Earth*, **114**, B01206.
- Poland, M. P., Fink, J. H. & Tauxe, L. (2004). Patterns of magma flow in segmented silicic dykes at Summer Coon volcano, Colorado: AMS and thin section analysis. *Earth and Planetary Science Letters* **219**, 155–169.
- Pollard, D. D. (1973). Derivation and evaluation of a mechanical model for sheet intrusions. *Tectonophysics* **19**, 233–269.
- Pollard, D. D. (1976). On the form and stability of open hydraulic fractures in the Earth's crust. *Geophysical Research Letters* **3**, 513–516.
- Pollard, D. D. (1987). Elementary fractures mechanics applied to the structural interpretation of dykes. In: Halls, H. C. & Fahrig, W. H. (eds) *Mafic Dyke Swarms. Geological Association of Canada Special Papers* **34**, 112–128. Geological Association of Canada, Canada.
- Queneau, A. L. (1902). Size of grain in igneous rocks in relation to the distance from the cooling wall. *School of Mines Quarterly, New York* **23**, 181–195.
- Quinn, A. W. (1943). Settling of heavy minerals in a granodiorite dyke at Bradford, Rhode Island. *American Mineralogist* **28**, 272–281.
- Rivalta, E., Taisne, B., Bunger, A. P. & Katz, R. F. (2015). A review of mechanical models of dyke propagation: Schools of thought, results and future directions. *Tectonophysics* **638**, 1–42.
- Romano, R. (1982). Succession of the volcanic activity in the Etnan area. *Memorie della Società Geologica Italiana* **23**, 27–48.
- Rubin, A. M. (1995). Propagation of magma-filled cracks. *Annual Review of Earth and Planetary Sciences* **23**, 287–336.
- Russ, J. C. & DeHoff, R. T. (1986). *Practical Stereology*. Plenum, 381 pp.
- Rust, A. C., Manga, M. & Cashman, K. V. (2003). Determining flow type, shear rate and shear stress in magmas from bubble shapes and orientations. *Journal of Volcanology and Geothermal Research* **122**, 111–132.
- Scarlato, P., Mollo, S., Blundy, J. D., Iezzi, G. & Tiepolo, M. (2014). The role of natural solidification paths on REE partitioning between clinopyroxene and melt. *Bulletin of Volcanology* **76**, 810.
- Serra, J. (1982). *Image Analysis and Mathematical Morphology*. Academic Press, 610 pp.
- Shelley, D. (1985). Determining paleo-flow directions from groundmass fabrics in the Lyttelton radial dykes, New Zealand. *Journal of Volcanology and Geothermal Research* **25**, 69–79.
- Sigurdsson, H. (2000). The history of volcanology. In: Sigurdsson, H., Houghton, B., Rymer, H., Stix, J. & McNutt, S. (eds) *The Encyclopedia of Volcanoes*, 1st edn. Academic Press, pp. 15–37.
- Sijbers, J. & Postnov, A. (2004). Reduction of ring artifacts in high resolution micro-CT reconstructions. *Physics in Medicine and Biology* **49**, 247–253.
- Spence, D. A. & Turcotte, D. L. (1990). Buoyancy-driven magma fracture, a mechanism for ascent through the lithosphere and the emplacement of diamonds. *Journal of Geophysical Research* **95**, 5133–5139.
- Spera, F. J. (1980). Aspects of magma transport. In: Hargraves, R. B. (ed.) *Physics of Magmatic Processes*. Princeton University Press, pp. 232–265.
- Spillaert, N., Allard, P., Métrich, N. & Sobolev, A. V. (2006). Melt inclusion record of the conditions of ascent, degassing, and extrusion of volatile-rich alkali basalt during the powerful 2002 flank eruption of Mount Etna (Italy). *Journal of Geophysical Research* **111**, B04203.
- Taisne, B. & Jaupart, C. (2009). Dyke propagation through layered rocks. *Journal of Geophysical Research* **114**, B09203.
- Taisne, B., Tait, S. & Jaupart, C. (2011). Conditions for the arrest of a vertical propagating dyke. *Bulletin of Volcanology* **73**, 191–204.
- Tanguy, J. C., Condomines, M. & Kieffer, G. (1997). Evolution of Mount Etna: constraints on the present feeding system and eruptive mechanism. *Journal of Volcanology and Geothermal Research* **75**, 221–250.
- Tanguy, J. C., Condomines, M., Le Goff, M., Chillemi, V., La Delfa, S. & Patané, G. (2007). Mount Etna Eruption of the last 2,750 years: revised chronology and location through archeomagnetic and ^{226}Ra – ^{230}Th dating. *Bulletin of Volcanology* **70**, 55–83.
- Tartese, R. & Boulvais, P. (2010). Differentiation of peraluminous leucogranites 'en route' to the surface. *Lithos* **114**, 353–368.
- Teall, J. J. H. (1884). Petrological notes on some north-of-England dykes. *Quarterly Journal of the Geological Society of London* **40**, 209–247.
- Vetere, F., Iezzi, G., Behrens, H., Cavallo, A., Misiti, V., Dietrich, M., Knipping, J., Ventura, G. & Mollo, S. (2013). Intrinsic solidification behaviour of basaltic to rhyolitic melts: A cooling rate experimental study. *Chemical Geology* **354**, 233–242.
- Vetere, F., Iezzi, G., Behrens, H., Holtz, F., Ventura, G., Misiti, V., Cavallo, A., Mollo, S. & Dietrich, M. (2015a). Glass forming ability and crystallization behaviour of sub-alkaline silicate melts. *Earth-Science Reviews* **150**, 25–44.
- Vetere, F., Mollo, S., Giacomo, P. P., Iezzi, G., Coltorti, M., Ferlito, C., Holtz, F., Perugini, D. & Scarlato, P. (2015b). Experimental constraints on the origin of pahoehoe 'cicirara' lavas at Mt. Etna Volcano (Sicily, Italy). *Bulletin of Volcanology* **77**, 44.
- Vona, A., Romano, C., Dingwell, D. B. & Giordano, D. (2011). The rheology of crystal-bearing basaltic magmas from Stromboli and Etna. *Geochimica et Cosmochimica Acta* **75**, 3214–3236.
- Wada, Y. (1992). Magma flow directions inferred from preferred orientations of phenocrysts in a composite feeder dyke, Miyake-Jima, Japan. *Journal of Volcanology and Geothermal Research* **49**, 119–126.
- Walter, J. M., Iezzi, G., Albertini, G., Gunter, M. E., Piochi, M., Ventura, G., Jansen, E. & Fiori, F. (2013). Enhanced crystal fabric analysis of a lava flow sample by neutron texture diffraction: A case study from the Castello d'Ischia dome. *Geochemistry, Geophysics, Geosystems* **14**, 179–196.
- Weickert, J. (1998). *Anisotropic Diffusion in Image Processing*. Teubner.
- Whitam, F., Blundy, J. & Kohn, S. C. (2012). SolEx: A model for mixed COHSCL-volatile solubilities and exsolved gas compositions in basalt. *Computers and Geosciences* **45**, 87–97.

- Winkler, H. G. F. (1948). Crystallization of basaltic magma as recorded by variation of crystal-size in dykes. *Mineralogical Magazine* **28**, 557–574.
- Wright, H. M. N. & Weinberg, R. F. (2009). Strain localization in vesicular magma: Implications for rheology and fragmentation. *Geology* **37**, 1023–1026.
- Yamato, P., Tartèse, R., Duretz, T. & May, D. A. (2012). Numerical modelling of magma transport in dykes. *Tectonophysics* **526**, 97–109.
- Yamato, P., Duretz, T., May, D. A. & Tartèse, R. (2015). Quantifying magma segregation in dykes. *Tectonophysics* **660**, 132–147.
- Zandomeneghi, D., Voltolini, M., Mancini, L., Brun, F., Dreossi, D. & Polacci, M. (2010). Quantitative analysis of X-ray microtomography images of geomaterials: Application to volcanic rocks. *Geosphere* **6**, 793–804.
- Zhang, T. T., Yan, E. C., Hu, X. M., & Cao, Y. B. (2012). Fractal description of rock mass structure representative elementary volume. *Advanced Materials Research* **594–597**, 439–445.
- Zuan Chen, Z., Jin, Z. H. & Johnson, S. E. (2011). Transient dyke propagation and arrest near the level of neutral buoyancy. *Journal of Volcanology and Geothermal Research* **203**, 81–86.

